



Studying polar lows over the Nordic Seas with satellite data

Anne-Marlene Blechschmidt



Hinweis

Die Berichte zur Erdsystemforschung werden vom Max-Planck-Institut für Meteorologie in Hamburg in unregelmäßiger Abfolge herausgegeben.

Sie enthalten wissenschaftliche und technische Beiträge, inklusive Dissertationen.

Die Beiträge geben nicht notwendigerweise die Auffassung des Instituts wieder.

Die "Berichte zur Erdsystemforschung" führen die vorherigen Reihen "Reports" und "Examensarbeiten" weiter.



Notice

The Reports on Earth System Science are published by the Max Planck Institute for Meteorology in Hamburg. They appear in irregular intervals.

They contain scientific and technical contributions, including Ph. D. theses.

The Reports do not necessarily reflect the opinion of the Institute.

The "Reports on Earth System Science" continue the former "Reports" and "Examensarbeiten" of the Max Planck Institute.

Anschrift / Address

Max-Planck-Institut für Meteorologie
Bundesstrasse 53
20146 Hamburg
Deutschland

Tel.: +49-(0)40-4 11 73-0
Fax: +49-(0)40-4 11 73-298
Web: www.mpimet.mpg.de

Layout:

Bettina Diallo, PR & Grafik

Titelfotos:

vorne:

Christian Klepp - Jochem Marotzke - Christian Klepp

hinten:

Clotilde Dubois - Christian Klepp - Katsumasa Tanaka

Studying polar lows over the Nordic Seas with satellite data

Dissertation zur Erlangung des Doktorgrades der Naturwissenschaften
im Departement Geowissenschaften der Universität Hamburg
vorgelegt von

Anne-Marlene Blechschmidt

aus Hamburg

Hamburg 2009

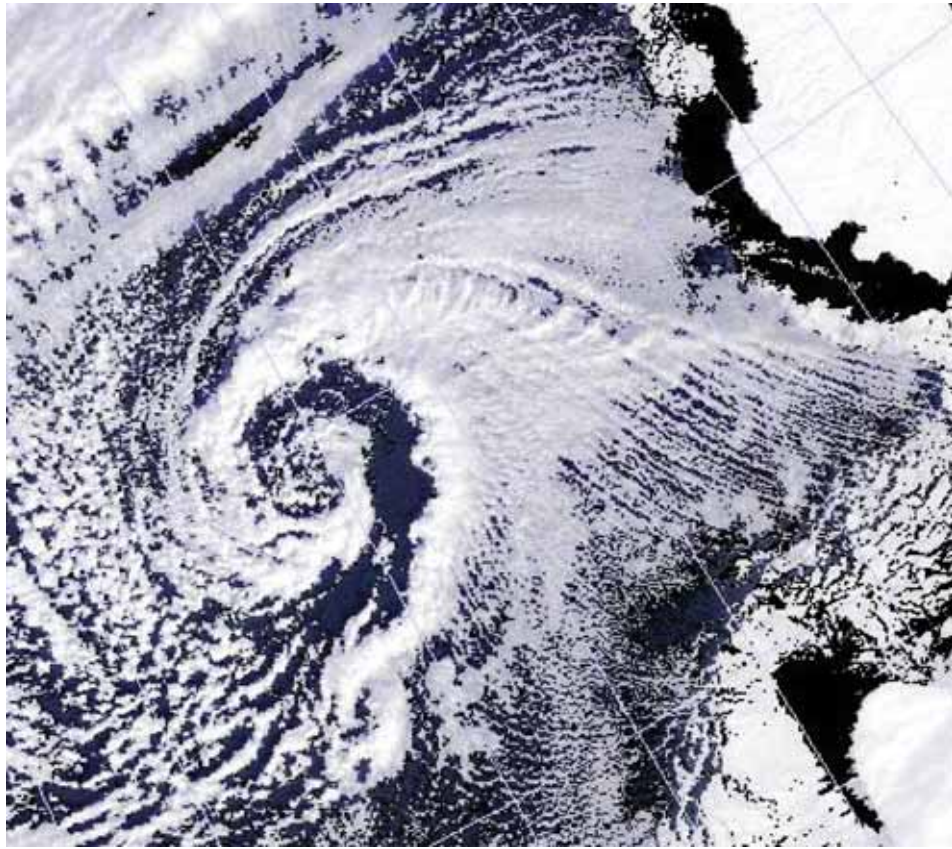
Anne-Marlene Blechschmidt
Max-Planck-Institut für Meteorologie
Bundesstrasse 53
20146 Hamburg
Germany

Als Dissertation angenommen
vom Department Geowissenschaften der Universität Hamburg

auf Grund der Gutachten von
Prof. Dr. Hartmut Graßl
und
Dr. Stephan Bakan

Hamburg, den 3. Februar 2009
Prof. Dr. Jürgen Oßenbrügge
Leiter des Departments für Geowissenschaften

Studying polar lows over the Nordic Seas with satellite data



MERIS satellite image of a polar low over the Barents Sea (Envisat, ESA)

Anne-Marlene Blechschmidt

Hamburg 2009

Contents

1	Introduction	7
2	2-year polar low climatology	13
3	Large-scale atmospheric circulation patterns during polar low events	15
4	Multi-sensor view of subsynoptic storm systems	17
4.1	Data	18
4.1.1	Ship observations	18
4.1.2	Active sensors	18
4.1.3	Passive sensors	19
4.2	Case 1: 15 March 2005	20
4.2.1	Initial development	20
4.2.2	Mature stage	22
4.2.3	Movement and the large scale circulation	25
4.2.4	Landfall	27
4.3	Case 2: 29 November 2005	30
4.3.1	Initial development	31
4.3.2	Mature stage	33
4.3.3	Large scale circulation	35
4.4	Case 3: 6 February 2006	36
4.4.1	Initial development	36
4.4.2	Mature stage	38
4.4.3	Large scale circulation	39
4.4.4	Reverse shear baroclinicity	40
4.5	Summary and concluding remarks	43
5	Comparison of satellite wind speeds and their error due to precipitation	47
5.1	Influence of rain and co-location methods	47
5.1.1	HOAPS-3	47
5.1.2	Dual frequency altimeters	48
5.1.3	QuikSCAT	49

Contents

5.2	Comparison of satellite derived wind speeds	49
5.3	Conclusions	52
6	Summary and conclusions	55
	Bibliography	59

1 Introduction

For centuries mariners of the Nordic Seas told tales about small violent storms developing out of nowhere to wreak havoc on the seas (*Renfrew, 2003*). Although these storm systems may cause substantial damage to coastal communities and are also believed to have caused a number of shipwrecks, it was not until the general availability of satellite imagery in the 1960s that it was realized that these phenomena are quite common (*Rasmussen and Turner, 2003*). As the satellite images indicated, the storms were maritime phenomena which tended to decline rapidly over land. For a long time no unique name existed for these small scale cyclones, due to their varying appearance. Some of the systems looked like comma clouds (see Figure 1.1) while others resembled small tropical cyclones with a cloud-free eye at their centers (see Figure 1.2). In one of the earliest references about the systems in question, *Dannevig (1954)* used the term “instability low” to suggest that they resulted from organized release of convective instability during outbreaks of cold air over relatively warm oceans. He produced a schematic chart that shows two instability lows embedded in the typical northerly airflow over the Norwegian Sea (see Figure 1.3). “Arctic bomb” or “Arctic hurricane” are further expressions that point to the rapid development and unusual strength of these systems. The most common nomenclature used today is “polar low”. This goes back to British meteorologists who noticed that polar lows could produce severe weather in the form of heavy snowfall around the British Isles (*Rasmussen and Turner, 2003*).

Since polar lows develop during outbreaks of cold air over relatively warm water, they occur most frequently during the winter months. A typical feature associated with these cold air outbreaks are fields of cumulus clouds which can be identified from satellite imagery. For example, such mesoscale cellular convection is evident to the west of the polar lows in Figure 1.1 and 1.2. The Nordic Seas region is prone to polar low development since strong temperature contrasts occur between regions covered by sea ice and the comparatively high oceanic temperatures associated with the Norwegian Current. However, it is known today that polar lows are a common feature of the relatively warm ice-free parts within the polar regions including not only the Nordic Seas but also the North Pacific, the Sea of Japan and the Labrador Sea. Some cases have also been reported for the Southern Hemisphere, e.g. in the region around New Zealand. Closer to the Antarctic continent however, the systems are generally much

1 Introduction

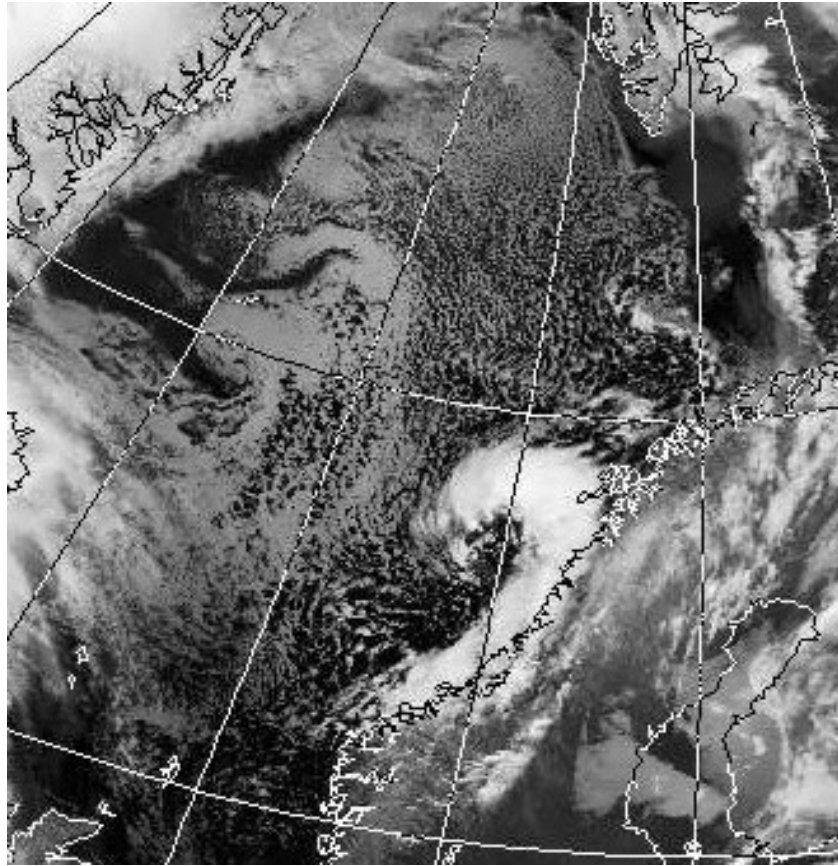


Figure 1.1: An AVHRR thermal infrared satellite image showing a comma shaped polar low near Norway on 13 January 2005 at 21:22 UTC. (Image courtesy of the NERC Satellite Receiving Station, University of Dundee, Scotland.)

weaker than their Northern Hemispheric counterparts, since the typical airflow is much more zonal and does not promote the large air-sea temperature differences that occur during cold air outbreaks in the Arctic (*Rasmussen and Turner, 2003*).

Polar lows show some similarities to tropical cyclones, since the transfer of heat from the ocean is regarded as an important factor for polar low development. However, polar lows that resemble tropical cyclones in appearance, i.e. deep convective spiral shaped polar lows with a clear eye at their center, have not been observed very often. Moreover, the systems are generally much weaker than their tropical counterparts (*Rasmussen, 1989*). One reason for their rareness is, that a vertical wind shear is often present over the high latitude oceans which prohibits the formation of an axisymmetric structure. Many polar lows form in the region of Arctic fronts which are characterized by strong low level baroclinicity occurring adjacent to the ice edge (*Reed, 1979*). Arctic fronts can often be traced from their origin at the ice edge as far as the coast of Norway (*Shapiro and Fedor,*

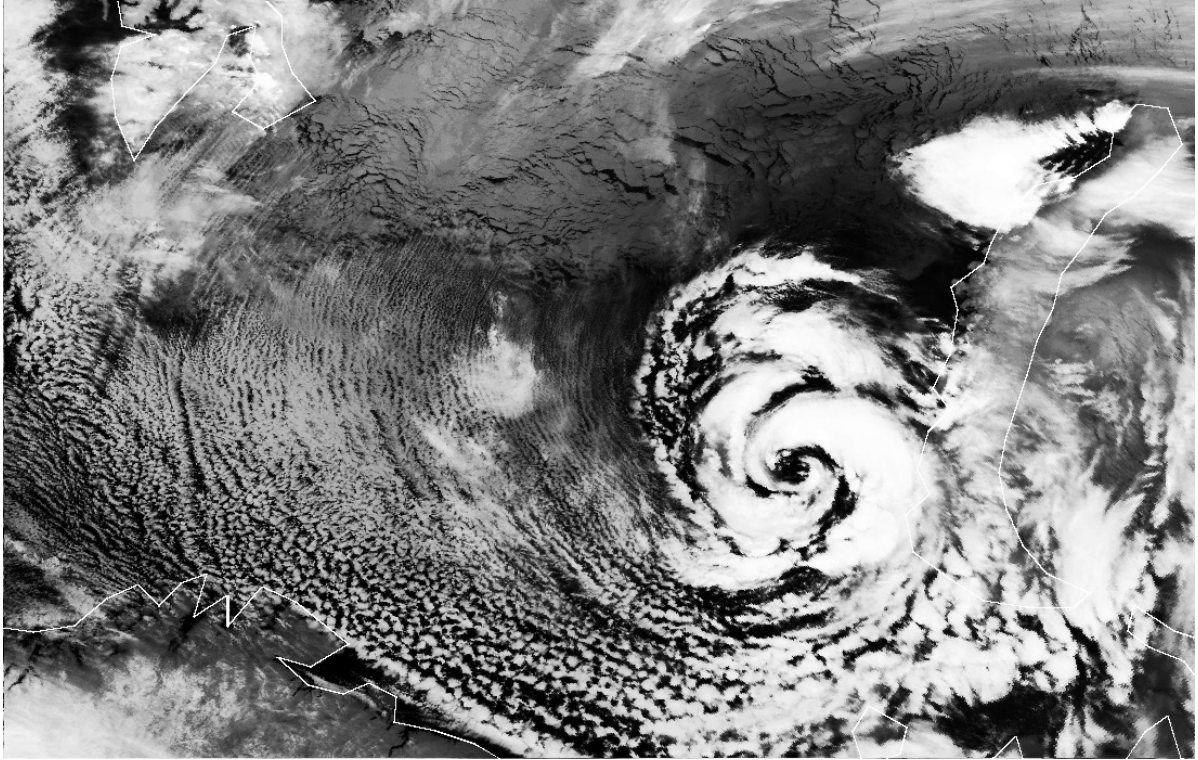


Figure 1.2: A Modis thermal infrared satellite image showing a hurricane like polar low over the Barents Sea on 20 December 2002 at 1:20 UTC. Note that the wind is aligned along the cloud streets seen to the west of the cyclone from the ice towards the open ocean. The sea ice is located in the upper part of the image to the north of the polar low.

1986). Nowadays, it is widely accepted that convective processes act together with baroclinic instability during the lifecycle of a polar low (e.g., *Bracegirdle and Gray, 2008*).

Advances in understanding polar lows resulted to a large extent from satellite observations (e.g., *Harold et al., 1999; Moore and Vonder Haar, 2003; Claud et al., 2004*), since meteorological in-situ data is sparse in the remote locations where polar lows form. The lack of in-situ data also complicates the initialization of numerical models. Furthermore, the small scale and short lifetimes of these systems represent a challenge to numerical forecasts. Nevertheless, modelling studies added valuable information about the physical mechanisms and meteorological conditions in which polar lows form. Over the last years, high resolution models have proven to be capable of reproducing polar lows (e.g., *Grønås and Kvamstø, 1995; Bracegirdle and Gray, 2008; Zahn et al., 2008*). However, there are still many open questions regarding the origin and lifecycle of polar lows and

1 Introduction

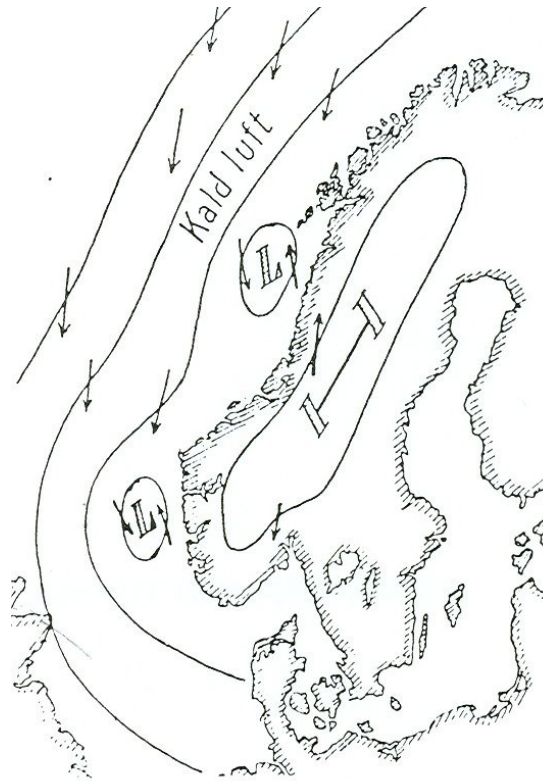


Figure 1.3: Schematic surface chart showing two instability lows near Norway (*Dannevig, 1954*).

researchers even discuss a possible impact of these small scale cyclones on the climate system. For example, *Condrón et al.* (2008) suggested a coupling between mesoscale cyclone activity over the Nordic Seas and changes in deep ocean circulation.

Nowadays, new possibilities for polar low research result from more sophisticated satellite remote sensing data. In this thesis, polar lows over the Nordic Seas are investigated by making use of this information from satellites. Within this work, a 2-year data set of polar low events has been compiled which is presented in chapter 2. It will be shown that gaps connected with the detection of polar lows can be filled by including passive microwave wind speeds in a satellite based detection scheme. Wind speeds are essential for the definition of polar lows since they are a measure of the intensity of these cyclones. In contrast to in-situ data over the polar oceans, the satellite derived wind speeds are available with a reasonable spatial coverage as well as spatial and temporal resolution.

In chapter 3, the large scale circulation during polar low events is analysed based on the 2-year data set described above. At least to the author's knowledge, such an analysis has not been applied to the whole Nordic Seas region in any previous study. In chapter 4

individual polar low and polar mesocyclone cases are investigated in more detail. An improved insight into the structure and development of the storm systems is achieved through combined use of active and passive satellite remote sensing data. The focus of chapter 5 is on the accuracy of satellite derived wind speeds in severe storm systems including polar lows, atmospheric fronts and comma-clouds over the eastern North Atlantic Ocean. Passive microwave wind speeds are compared to wind speeds from active satellite remote sensors. Finally, the results of this thesis are summarized and discussed in chapter 6.

1 Introduction

2 2-year polar low climatology

This chapter is identical to the paper by *Blehschmidt* (2008) entitled “A 2-year climatology of polar low events over the Nordic Seas from satellite remote sensing”.

2 2-year polar low climatology

3 Large-scale atmospheric circulation patterns during polar low events

This chapter is identical to the paper by *Blechschmidt et al.* (2009) entitled “Large-scale atmospheric circulation patterns during polar low events over the Nordic seas”.

3 Large-scale atmospheric circulation patterns during polar low events

4 Multi-sensor view of subsynoptic storm systems

The characteristics of polar lows, such as their geographical and temporal distribution, their intensity, as well as the large scale circulation during polar low events, have been studied in the preceding chapters. The purpose of this chapter is to achieve a more detailed view of the development of individual subsynoptic storm systems over the Norwegian Sea by making combined use of several active and passive satellite remote sensors as well as ship observations. This combined approach incorporates information from several levels in the atmosphere starting from the winds that the storm systems cause on the ocean surface up to the cloud tops. In addition, NCEP Reanalysis data is used to characterize the large scale conditions under which the cyclones form. These large scale conditions are compared to the characteristic large scale patterns that were described in chapter 3. The cases for which a comparably large number of coinciding observations from active and passive satellite remote sensors are available are rare. Three of these rare cases are discussed below: two polar low events and also a polar mesocyclone event that does not completely fulfil the definition of the term “polar low” by *Rasmussen and Turner (2003)*.

The first case investigated is a dual polar low event on 15 March 2005 which is unique in the wealth of different data sources available. The passes of several satellites coincide not only over the genesis area of the polar lows but also in their observation time. Since wind speeds exceeding 15 m/s were only derived from two instantaneous SSM/I observations, this rather weak event was not regarded as a polar low in the 2-year data set described in chapter 2. However, the wind speed criterion for polar lows is fulfilled by satellite wind speeds derived from active remote sensing systems. Therefore, it is referred to a polar low event throughout the present chapter.

The second case discussed below is a polar low event on 29 November 2005 which is selected from the 2-year polar low data set. Finally, a polar mesocyclone event on 6 February 2006 is investigated which developed due to reverse shear baroclinicity.

4.1 Data

In addition to the satellite data and NCEP Reanalyses described in chapter 2 and 3, ship observations as well as other data from active and passive satellite sensors are used to study the development of subsynoptic cyclones.

4.1.1 Ship observations

The VOS (Voluntary Observing Ship) scheme is an international programme comprising member countries of the WMO (World Meteorological Organization) that recruit ships to take and transmit meteorological observations whilst at sea. The VOS observations are archived in ICOADS (International Comprehensive Ocean-Atmosphere Data Set). This data set was obtained from the CISL Research Data Archive (<http://dss.ucar.edu/>).

4.1.2 Active sensors

The Jason-1 and Envisat altimeters are two out of four most recent dual-frequency altimeters which are currently in space (the others are TOPEX/Poseidon and Jason-2). The second frequency is aimed at the determination of the ionospheric electron content, which affects the radar signal path delay. Launched by the end of 2001, Jason-1 was the first follow-on to the TOPEX/Poseidon mission. The primary instrument is the Poseidon-2 altimeter which operates at 13.6 GHz (Ku band) and 5.3 GHz (C band). The second generation radar altimeter (RA-2), launched onboard the Envisat satellite in March 2002, emits pulses at S band (3.2 GHz) and Ku band. Altimeter measurements are limited to nadir observations and are primarily dedicated to ocean topography, e.g. significant wave height. However, wind speeds are also estimated through relationships with the Ku band backscatter coefficient. The footprint size of the altimeter observations is a few kilometers. All Envisat data used in this thesis was provided by the European Space Agency through a Category-1 project (Project ID: 3898) which was granted to the author in 2006. The Jason-1 and the QuikSCAT data, which are described below, were obtained from the Physical Oceanography Distributed Active Archive Center at the NASA Jet Propulsion Laboratory (<http://podaac.jpl.nasa.gov>).

An ASAR (Advanced Synthetic Aperture Radar) operating at C band is another payload onboard the Envisat satellite. Compared to the ERS SAR mission, ASAR offers several improvements including increased swath coverage and higher spatial resolution. In this study ASAR wind speeds with an approximate coverage of 400 x 400 km and a resolution of 300 m were used. The wind speeds were provided by Jochen Horstmann (former staff

of the GKSS Research Center) who processed the wind speeds with WISAR (Wind Retrieval from Synthetic Aperture Radar, http://www.gkss.de/institute/coastal_research/structure/system_analysis/KSD/projects/wisar/index.html).

The SeaWinds scatterometer was launched in June 1999 onboard the QuikSCAT satellite. SeaWinds is a microwave radar that collects near surface wind speed and direction from backscattered power at Ku band via dual pencil beam scans at 46° and 55° incidence angles. Like the Envisat and Jason-1 altimeter, the SeaWinds scatterometer retrieves wind speeds through a relation with the Ku band backscatter coefficient. The wind speed data used in this thesis has a resolution of 25 km.

4.1.3 Passive sensors

The AATSR (Advanced Along-Track Scanning Radiometer) onboard the Envisat satellite measures reflected and emitted radiation at several wavelengths between $0.55 \mu\text{m}$ and $12 \mu\text{m}$. This instrument was primarily designed to measure SST. However, cloud top temperature is also available from the Level 2 full resolution geophysical product and is used in this thesis. AATSR data has a resolution of 1 km at nadir.

The AMSR-E (Advanced Microwave Scanning Radiometer) is a passive-microwave radiometer onboard the Aqua satellite which was launched in May 2002. It measures brightness temperatures in 12 channels and 6 frequencies between 6.9 GHz and 89.0 GHz. Gridded AMSR-E SST with a resolution of 25 km was obtained from the MISST (Multi-sensor Improved Sea Surface Temperature) project through their web site (<http://www.misst.org/>).

MODIS Level-1 data is used in addition to the operational MODIS Level-2 cloud product which was described in chapter 2. Thermal infrared satellite images are produced from the MODIS Level-1 data which has a resolution of 1 km. Although mainly AVHRR quiklook images from the NERC Satellite Receiving Station have been used to study the development of the cyclones, only MODIS satellite images will be displayed for two of the three subsynoptic storm systems described below. This is done because the precise location of ships and altimeter tracks can be overlaid on the MODIS satellite images. (All MODIS data was retrieved from <http://modis.gsfc.nasa.gov/>.)

Instead of the gridded HOAPS data described in chapter 2, the HOAPS-S data set is used in the present chapter. The HOAPS-S data set contains all retrieved physical parameters in the original SSM/I scan resolution (that is 50 km for wind speed, precipitation and latent heat flux) for every individual satellite. It is intended for the use in case studies or comparison experiments (<http://www.hoaps.org/>).

4.2 Case 1: 15 March 2005

In the early morning of 15 March 2005 two comma shaped polar lows developed over the Norwegian Sea. The thermal infrared MODIS satellite image in the top right panel of Figure 4.1 shows the polar lows in their mature stage at 10:50 UTC. This polar low event was spotted by a wealth of satellite sensors, especially during their mature stage and in the evening when the southern polar low made landfall. In the following the initial development of both systems is discussed first, followed by their mature stage and movement as well as the large scale circulation during this polar low event. Finally, the landfall of the southern polar low is described. The southern polar low is termed “SPL”, while the northern polar low is termed “NPL”.

4.2.1 Initial development

The sequence of MODIS images in Figure 4.1 illustrates the lifecycle of the polar lows as well as the conditions prior to their development. In the evening of 13 March 2005 (top left panel of Figure 4.1), a cloud band was located over the Norwegian Sea that connected a large scale low pressure system which was situated over the Barents Sea with a large scale low located over the Shetland Islands. A cold air outbreak is visible to the north of this cloud band as evidenced by the small scale cumulus clouds.

In the evening of 14 March 2005 (center left panel of Figure 4.1), the two large scale lows had decayed, while the cloud band remained located over the Norwegian Sea and formed a nearly stationary front. Note that at this time, the southern part of the stationary front was cut off from the rest of the front. Later, SPL developed out of this southern part which is located at 0° East and 65° North. Moreover, during 14 March 2005 two polar mesocyclones had developed from the center of the decaying large scale low over the Barents Sea. These small scale vortices, which rotated in a cyclonic sense around each other, propagated towards the northern part of the stationary front. It follows from the inspection of NCEP R-2 data that the two polar mesocyclones were part of a large scale upper level cold low that moved from the Barents Sea towards the Norwegian Sea. The large scale circulation during the dual polar low event will be described in more detail in section 4.2.3.

During the early hours of 15 March 2005 (bottom left panel of Figure 4.1) the northern part of the stationary front got involved into the cyclonic rotation of the two polar mesocyclones. Later, this northern part of the stationary front grew to NPL. At 15 March 2005 10:50 UTC (top right panel of Figure 4.1) the two polar lows had fully developed.

4.2 Case 1: 15 March 2005

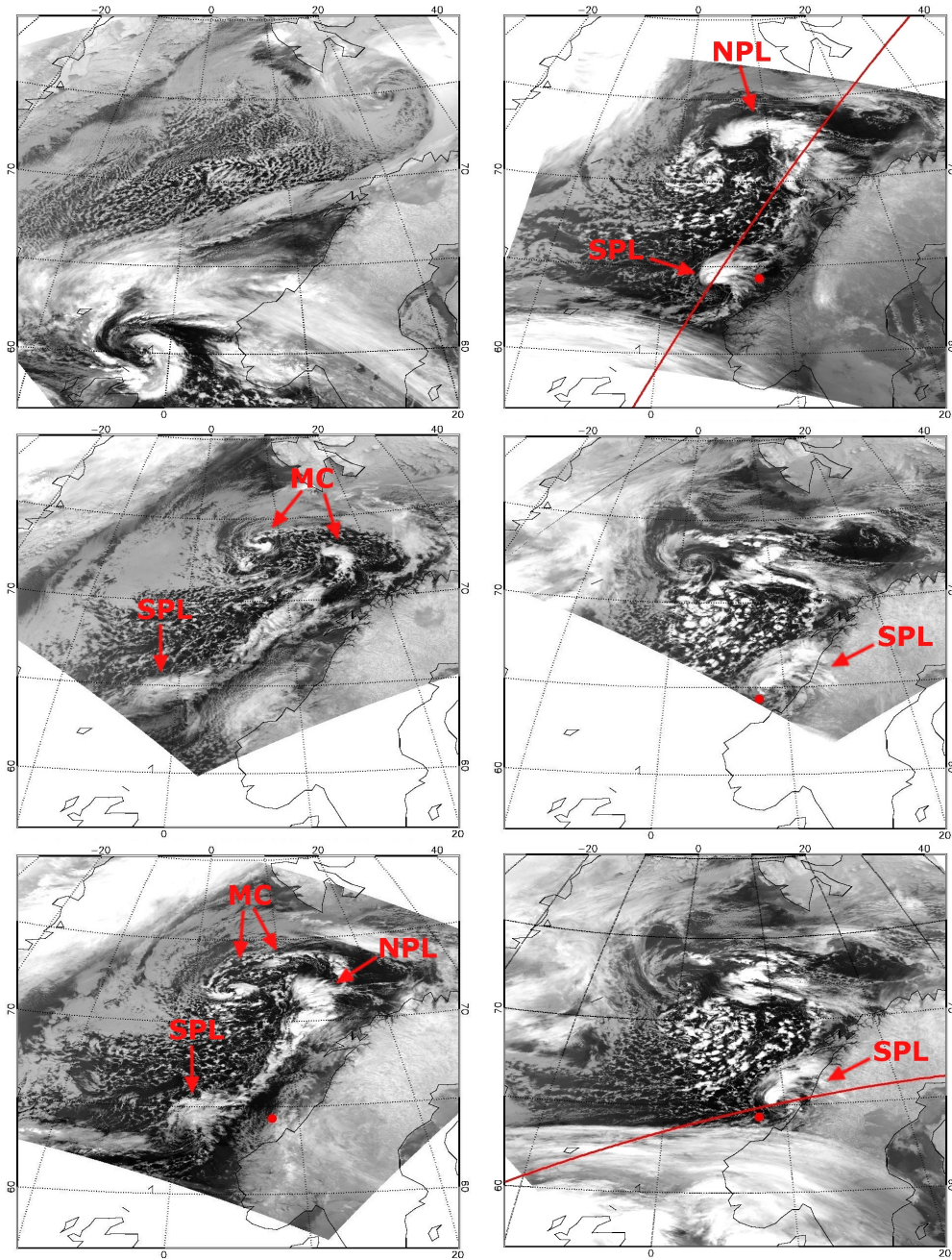


Figure 4.1: MODIS thermal infrared satellite images showing the lifecycle of the polar lows as well as the conditions prior to their development (top left: 20:45 UTC 13 March 2005; center left: 19:50 UTC 14 March 2005; bottom left: 3:00 UTC 15 March 2005; top right: 10:50 UTC 15 March 2005; center right: 18:55 UTC 15 March 2005; bottom right: 20:35 UTC 15 March 2005). The red circles mark the location of ship Draugen at the time closest to the MODIS observations. The red lines represent altimeter tracks (top right: Envisat at 10:55 UTC 15 March 2005; bottom right: Jason-1 at 20:30 UTC 15 March 2005). MC stands for “mesocyclone”, NPL for “northern polar low” and SPL for “southern polar low”.

4 Multi-sensor view of subsynoptic storm systems

The genesis of the polar lows described above is in agreement with several studies according to which an important factor for triggering polar lows is the approach of a cold upper level low or trough. For example, *Rasmussen and Turner (2003)* noted that when a large scale, cold core upper level vortex is situated over the sea, polar lows may form in the central part of the low, as well as in the region of cyclonic, upper level flow along the rim of the cyclone. This is most likely due to the action of small scale upper level troughs embedded within the flow. Overall, there are strong indications that the genesis of the two polar lows was triggered by a mobile upper level cold low.

4.2.2 Mature stage

Figure 4.2 shows fields of several atmospheric parameters closest to the mature stage of the polar lows as derived from HOAPS and MODIS data. NPL reached wind speeds up to 16 m/s, precipitation rates up to 2 mm/hr, latent heat fluxes up to $170 W/m^2$ and cloud top temperatures down to 220 K. The latter corresponds to a cloud top pressure (not shown) of 330 hPa as derived from MODIS data. SPL reached HOAPS wind speeds of 14.5 m/s, precipitation rates up to 3 mm/hr and latent heat fluxes up to $230 W/m^2$. The same minimum cloud top temperature and minimum cloud top pressure values as for NPL were derived for SPL. Regarding the frequency distributions of all these atmospheric parameters for polar lows detected in 2004 and 2005 shown in Figure 4 of chapter 2, NPL does not reach the strength of the majority of polar lows. The precipitation rates reached by SPL are larger than those for most polar lows, while the latent heat fluxes are a bit lower than those for most polar lows. SPL does not fulfill the wind speed criterion for polar lows during its mature stage. However, the wind speed criterion is fulfilled later on 15 March 2005 during the landfall of SPL as will be described below.

The mature stage of the polar lows was also observed by the Envisat altimeter. Figure 4.3 (a) shows horizontal profiles of atmospheric parameters from the Envisat altimeter as well as from HOAPS and MODIS data along the track of the Envisat altimeter. The corresponding altimeter track is shown in the top right panel of Figure 4.1. The track crossed the center of SPL and the tail of NPL. Significant wave height reaches maxima of about 9 m to the south and to the north of NPL. Envisat altimeter wind speeds close to 15 m/s and 13 m/s are reached for SPL and NPL, respectively. The location of maxima in HOAPS wind speed, precipitation and latent heat flux as well as the location of the minima of MODIS cloud top temperature (indicative of the high cloud walls close to the center of the polar lows) agree very well with the Envisat altimeter wind speed profile. Moreover, the maxima of HOAPS and Envisat altimeter wind speed associated with the two polar lows, agree well in magnitude. However, HOAPS

reaches mostly higher values than the Envisat altimeter for altimeter wind speeds lower than approximately 7 m/s. This is in agreement with the results of chapter 5, where a more detailed comparison between HOAPS and Envisat altimeter wind speeds will be presented.

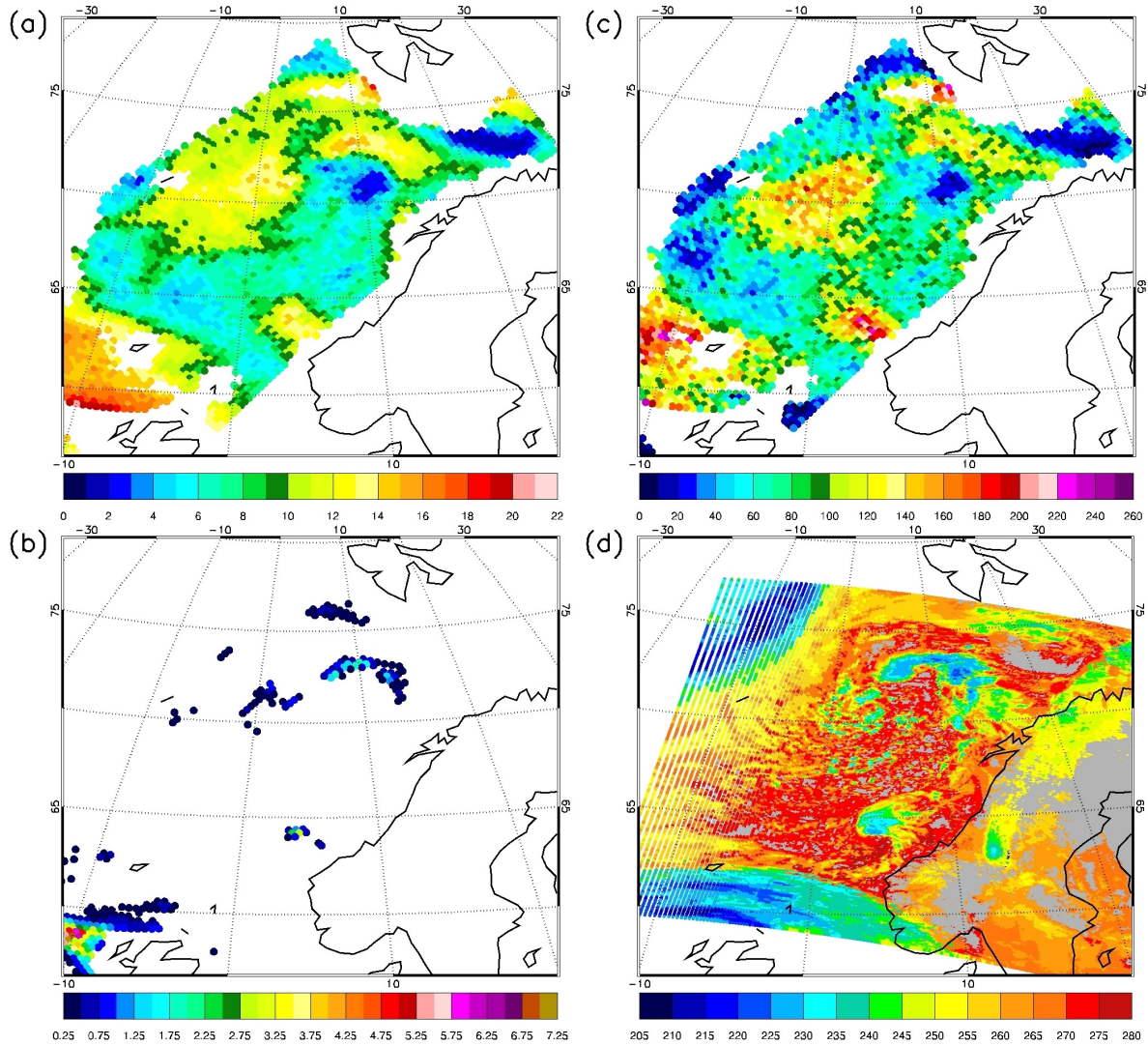


Figure 4.2: Satellite derived atmospheric parameters on 15 March 2005 corresponding to the mature stage of the polar lows showing (a) wind speed [m/s], (b) precipitation [mm/hr], (c) latent heat flux [W/m^2] from HOAPS (DMSF F15) at 10:45 UTC and (d) cloud top temperature [K] from MODIS at 10:50 UTC.

4 Multi-sensor view of subsynoptic storm systems

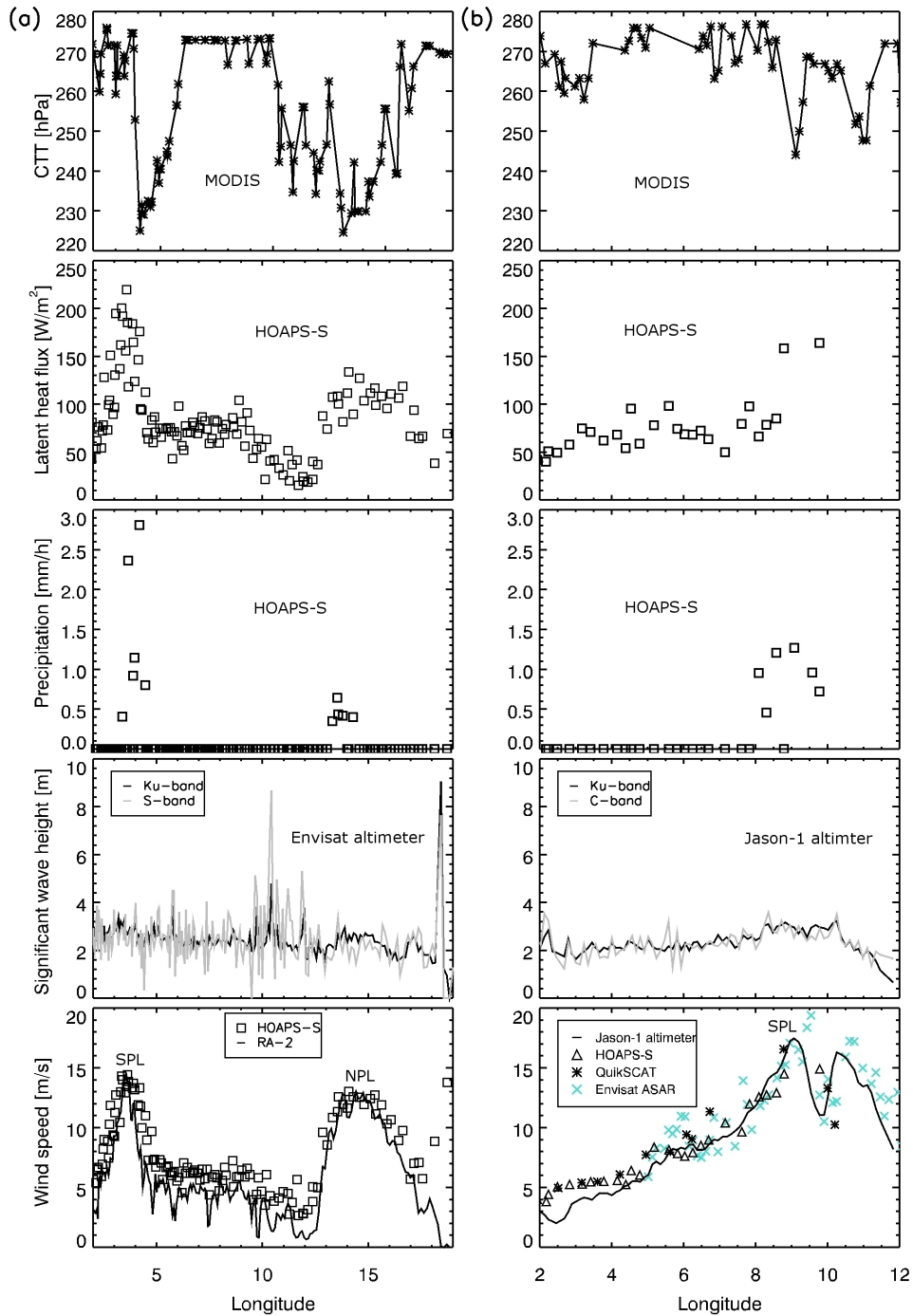


Figure 4.3: Satellite derived atmospheric parameters for (a) the Envisat altimeter track at 10:55 UTC 15 March 2005 shown in the top right panel of Figure 4.1 and (b) the Jason-1 altimeter track at 20:30 UTC 15 March 2005 shown in the bottom right panel of Figure 4.1. For MODIS cloud top temperature (top panels) and ASAR wind speed (bottom right panel) every value that lies within a circle of 2.5 km and 0.15 km radius from the center of the altimeter footprint is shown, respectively. For QuikSCAT (bottom right panel) and HOAPS data (second to third panels from above and bottom panels) values within a circle of 22.5 km and 10 km are shown, respectively.

4.2.3 Movement and the large scale circulation

Figure 4.4 shows the tracks of the polar low pair as determined from AVHRR images. The tracks exhibit a counter clockwise rotation with NPL moving away- and SPL moving towards the Norwegian coast. This cyclonic motion agrees well with the NCEP R-2 sea level pressure field at 6:00 UTC 15 March 2005 (see Figure 4.5) which corresponds to the mature stage of the polar lows. The sea level pressure field shows a large scale surface low over the Norwegian Sea. This NCEP field as well as the thermal infrared satellite image at 10:50 UTC 15 March 2005 (top right panel of Figure 4.1) suggests that the polar lows were part of one complex low pressure system with several low pressure cores. Three vortices can be identified from the satellite image: two associated with the polar lows in their mature stage and one located near 3° East and 71° North. The latter is associated with the western one of the two polar mesocyclones that triggered the polar low development as described in section 4.2.1. Such cloud signatures with multiple mesoscale cyclones revolving around a common center have been termed “merry-go-round” systems by *Forbes and Lottes (1985)*. According to *Businger and Reed (1989)* mesocyclones that are part of merry-go-round systems are to a first approximation advected by the large scale flow.

Figure 4.4 also shows the SST distribution derived from AMSR-E ascending passes on 15 March 2005. There is warmer water along the coast of Norway. This is due to the Norwegian current which flows northwards along the coast of Norway and also into the Barents Sea. While NPL experienced a decrease of SST as it moved westwards, the eastwards moving SPL experienced an increase of SST of about 4°C .

Rasmussen (1979) investigated the impact of increasing SST along the path of polar lows that form over the southern part of the Norwegian Sea. He concluded that when the air is streaming eastwards towards the coast of Norway, conditional instability of the second kind (CISK) is a possible explanation for the formation of polar lows in this area. Due to the increasing SST, the lapse rate in the lower atmosphere becomes more unstable and the equivalent potential temperature for the surface air increases. As the density of the vertical column is determined by equivalent potential temperature of the rising surface air, this may cause a decrease of surface pressure.

It would require detailed numerical simulations to determine the exact dynamical process which caused the genesis of NPL and SPL. However, the fact that the maximum latent heat fluxes derived from HOAPS close to the mature stage of both polar lows are 60 W/m^2 larger for SPL compared to NPL (see above) supports the conclusion that air-sea interaction might have contributed considerably to the intensification of SPL.

Regarding the classification system described in chapter 3, the dual polar low event refers to the class of western polar lows. The NCEP fields shown in Figure 4.5, which

4 Multi-sensor view of subsynoptic storm systems

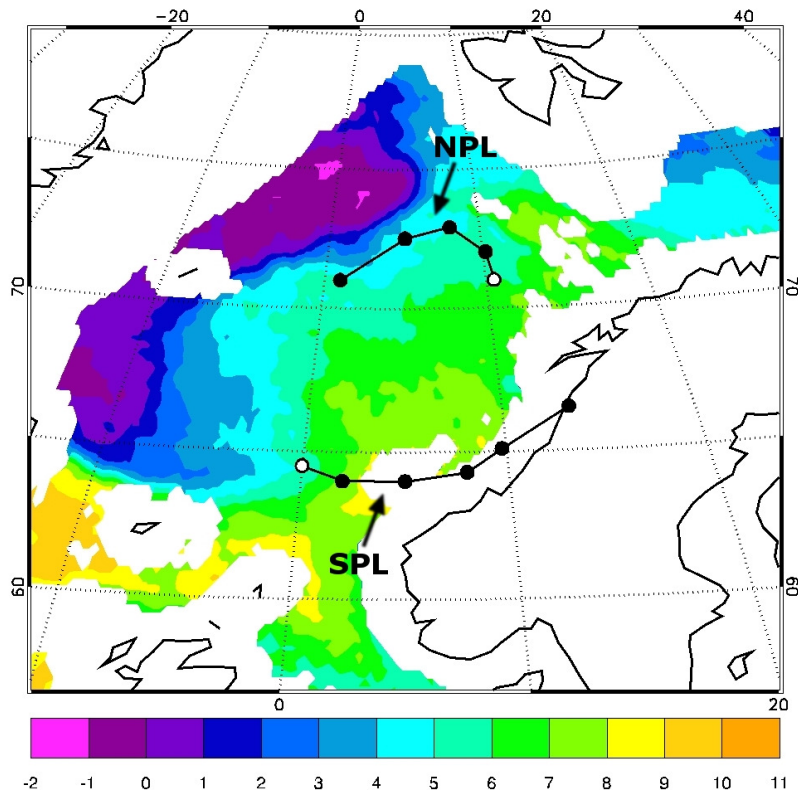


Figure 4.4: SST [K] from AMSR-E ascending passes for 15 March 2005. The tracks of the polar lows determined from AVHRR images are also given. The white circles represent the genesis regions of the polar lows. NPL stands for “northern polar low” and SPL for “southern polar low”

correspond to the mature stage of the polar low pair, agree well with the schematic chart of the large scale circulation during western polar low events (see top left panel of Figure 6 in chapter 3). A large scale low is situated over the Norwegian Sea and a high is situated over Greenland. This results in a northerly surface flow over the Norwegian Sea. A SKT- T_{500} difference of up to 52 K has developed over the genesis region of the polar lows. This difference is associated with the arrival of the upper level cold low (see section 4.2.1) over a relatively warm ocean. The upper level low reaches a minimum GPH_{500} value of 5060 gpm and a minimum T_{500} value of 230 K. In consistency with the upper level NCEP R-2 fields, IPV_{315} derived from NCEP R-1 (not shown) reaches a value of 8 PVU in the center of the upper level disturbance. These minimum GPH_{500} , minimum SKT- T_{500} , minimum T_{500} and maximum IPV_{315} values are close to the values that are most often reached during polar low events (see Figure 5 in chapter 3).

Although the large scale fields described above agree well with the schematic chart for western polar low events, there is one specific difference regarding the movement of the

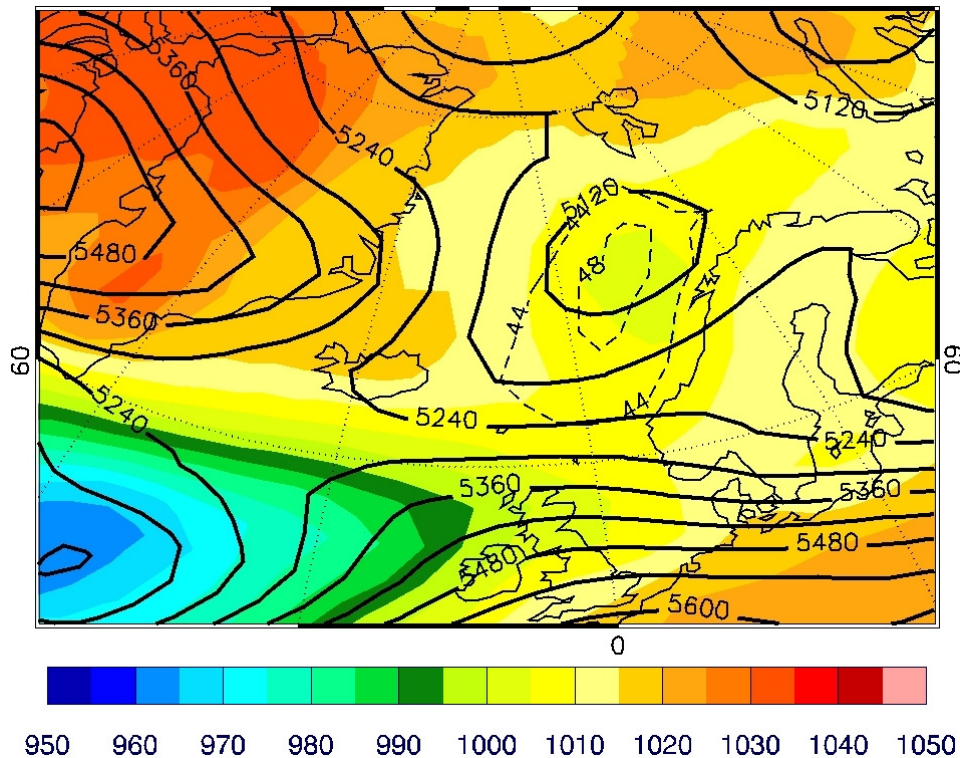


Figure 4.5: NCEP R-2 fields showing the large scale conditions during the polar low event on 15 March 2005 6:00 UTC. The coloured contours show sea level pressure [hPa], the black contours show GPH_{500} [gpm] and the black dashed contours show $SKT-T_{500} \geq 44K$.

upper level disturbance which was described in section 4.2.1. In contrast to the evolution of the polar low mean fields of GPH_{500} (see Animation 2 of *Blechsmidt et al.*, 2009), the development of NPL was not triggered by an upper level trough that originated from the Fram Strait, but by an upper level low originating from the Barents Sea. While the polar low mean fields by *Blechsmidt et al.* (2009) show the “mean” large scale circulation associated with western polar low events, the patterns associated with individual polar low events can deviate to some extent from the mean pattern. Moreover, it should be kept in mind that the dual polar low event discussed in this section is not included in the 2-year data set which was the basis for the study by *Blechsmidt et al.* (2009).

4.2.4 Landfall

In the evening of 15 March 2005, NPL already had decayed while SPL reached the coast of Norway (see center and bottom right panel of Figure 4.1).

4 Multi-sensor view of subsynoptic storm systems

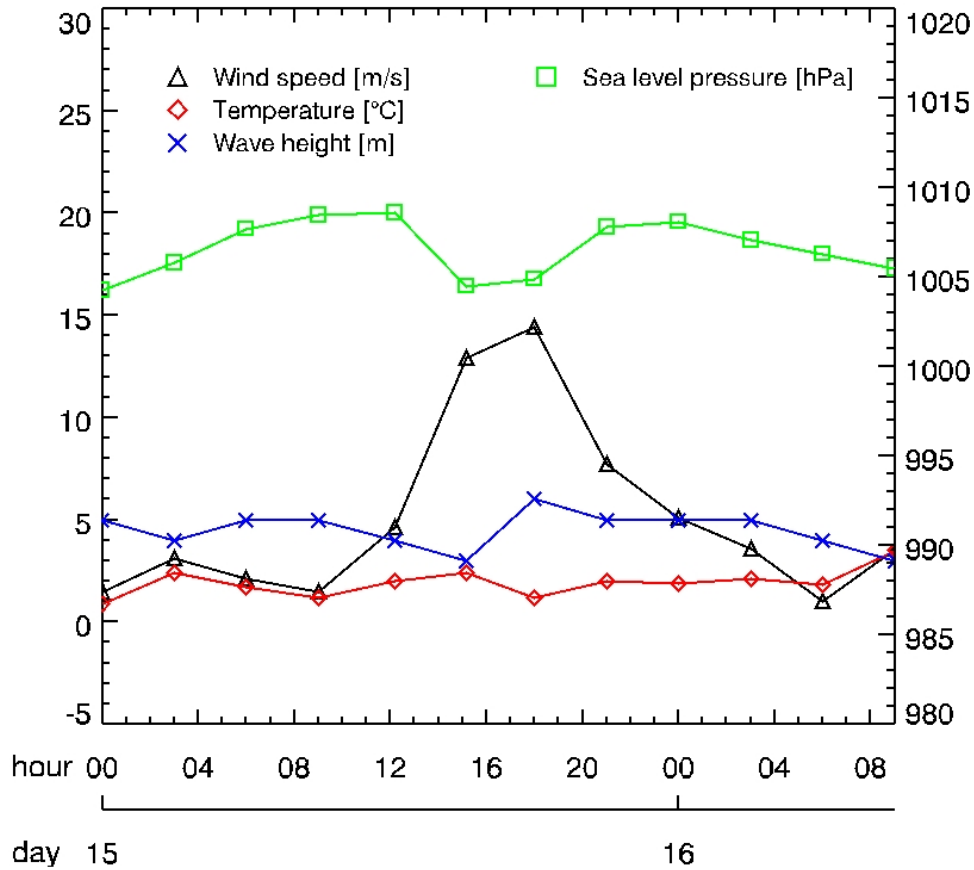


Figure 4.6: Observations from ship Draugen for 0:00 UTC 15 March 2005 to 8:00 UTC 16 March 2005 derived from VOS data.

Ship Draugen was hit by the center of SPL during its landfall. The position of the ship between 10:50 UTC and 20:35 UTC on 15 March 2005 is marked by a red circle in the right side panels of Figure 4.1. The observations from ship Draugen are shown in Figure 4.6. Between 12:00 UTC and 21:00 UTC on 15 March 2005 a pressure fall of about 4 hPa and a subsequent rise of the same magnitude was reported. The pressure minimum associated with the polar low reached a value of about 1005 hPa. The magnitude of the pressure minimum as well as the magnitude of the pressure fall are small compared to other polar low cases. For example, the pressure decreased by 12 hPa in 4 hours to a value of 987 hPa during a very prominent polar low event studied by *Claud et al.* (2004). In the present case, a maximum wind speed of 14 m/s and a wave height of 6 m was reached at 18:00 UTC. No significant maximum or minimum was reported for temperature which remained at around 2°C. The maximum wind speed from ship

Draugen is of the same magnitude as the maximum HOAPS and Envisat altimeter wind speeds derived at the mature stage of SPL. This suggests that the polar low did not intensify between approximately 10:50 UTC in the morning and 18:00 UTC in the evening.

An Envisat ASAR image is available for 20:45 UTC allowing the verification of the position of the cyclone center at sea level and the determination of high resolution wind speeds. The latter are shown in Figure 4.7 (a). HOAPS and Jason-1 altimeter wind speeds are overlaid on the Envisat ASAR wind field (the corresponding track of Jason-1 is shown in the bottom right panel of Figure 4.1). In addition, QuikSCAT wind speeds and wind directions are given in Figure 4.7 (b). The time difference between the HOAPS and QuikSCAT observations and the Envisat observation is almost two hours. However, the comparison of MODIS thermal infrared satellite images for 18:55 UTC (center right

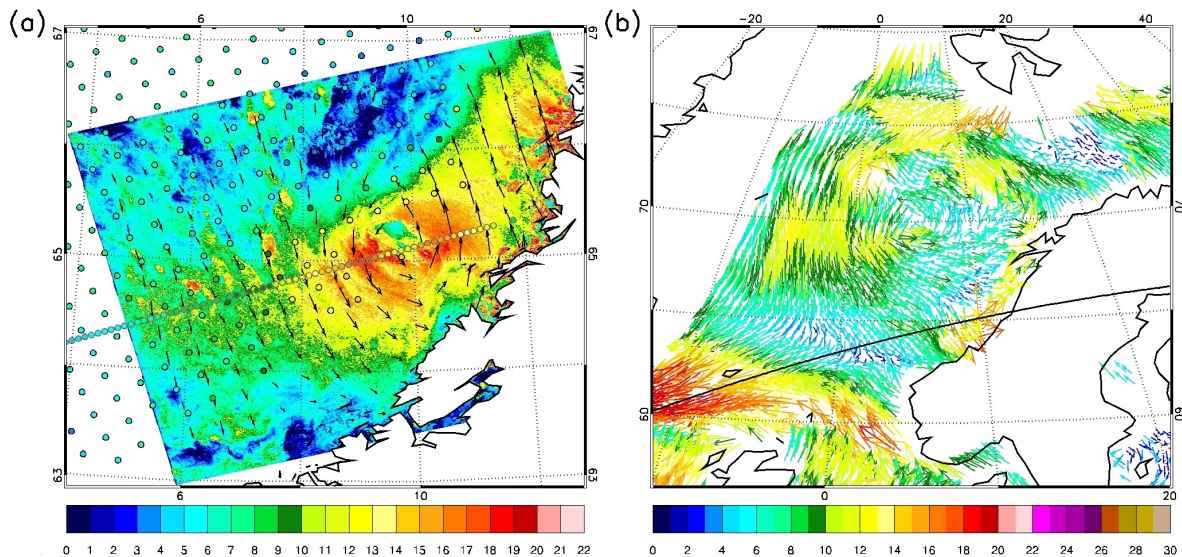


Figure 4.7: Satellite derived wind speeds [m/s] for the evening of 15 March 2005. Figure (a) shows wind speeds calculated from an Envisat ASAR WS image with the CMOD-IFR2 algorithm at 20:45 UTC. The resolution of the ASAR wind speeds is 300 m. The black arrows show wind directions from ASAR. The wind directions were interpolated from a resolution of 10 km to 300 m. The ASAR wind speeds and directions were kindly provided by Jochen Horstmann (former staff of the GKSS Research Center). Overlaid on the ASAR image are HOAPS wind speeds from DMSF F15 at 19:05 UTC (black encircled dots) and Jason-1 altimeter wind speeds at 20:30 UTC (grey encircled dots). Figure (b) shows wind speed and wind direction from QuikSCAT at 18:39 UTC. The black line shows the Jason-1 altimeter track at 20:30 UTC.

4 Multi-sensor view of subsynoptic storm systems

panel of Figure 4.1) and for 20:35 UTC (bottom right panel of Figure 4.1) shows that the polar low remained nearly stationary between these two satellite observation times. The time difference between Jason-1 altimeter and ASAR wind speeds is only about 10 minutes. There is a high level of agreement between the wind speeds derived from several satellites as shown in Figure 4.7. The ASAR wind speed data indicates that SPL had developed an eye-like structure at the sea level. The increase in wind speed close to the center of the polar low is detected by all sensors. The position of this eye-like structure agrees well with the cloud free regions in the center of the polar low seen by the MODIS satellite at 20:35 UTC (bottom right panel of Figure 4.1).

Figure 4.3 (b) shows horizontal profiles from Jason-1 as well as HOAPS, QuikSCAT, ASAR and MODIS data along the altimeter track. The eye is visible due to a rapid decrease in altimeter and ASAR wind speeds at approximately 10° East. Altimeter wind speeds of 18 m/s and ASAR wind speeds close to 21 m/s are reached near the center of the vortex. Since these values are higher than the wind speed maximum reported by ship Draugen for 18:00 UTC, this suggests that SPL had reintensified after 18:00 UTC. The decrease in wind speed at 10° East is not represented by the HOAPS data. HOAPS and QuikSCAT mostly reach larger values than the Jason-1 altimeter for altimeter wind speeds approximately lower than 12 m/s. As will be described in chapter 5, the deviations in wind speed basically result from different satellite observation times, resolutions and frequencies of the remote sensors. E.g., HOAPS wind speeds have a resolution of 50 km, while the footprint size of the Jason-1 altimeter is only a few kilometers. Note that to the east of the eye, no HOAPS data and only two QuikSCAT observations are available due to the proximity of the Norwegian coast. The decrease in MODIS cloud top temperature to the west and east of 10° East indicates the high cloud wall near the center of SPL. The locations of these minima agrees very well with the corresponding altimeter wind speed maxima. Significant wave heights of only 3.5 m are reached near the center of SPL. HOAPS precipitation rates of 1.3 mm/hr and latent heat fluxes of $170 W/m^2$ are reached to the west of the cyclone center. The maximum latent heat flux value is $50 W/m^2$ smaller than the $220 W/m^2$ maximum which was derived during the mature stage of SPL along the track of the Envisat altimeter (see Figure 4.3 (a)). This is consistent with the fact that the supply of heat and moisture from the ocean decreases when a polar low makes landfall.

4.3 Case 2: 29 November 2005

A western polar low formed on 29 November 2005 over the Norwegian Sea. The initial development of the polar low is described first, followed by the mature stage and the large scale circulation.

4.3.1 Initial development

The development of the polar low is illustrated by the MODIS thermal infrared images shown in Figure 4.8. In the early morning of 29 November 2005 at 1:55 UTC (top left panel of Figure 4.8) a cloud cluster was situated at 10° East and 70°N. The cluster resulted from a polar low event one day prior to the one described in this section. Small scale cumulus clouds are visible to the west and southwest of the cloud cluster indicating

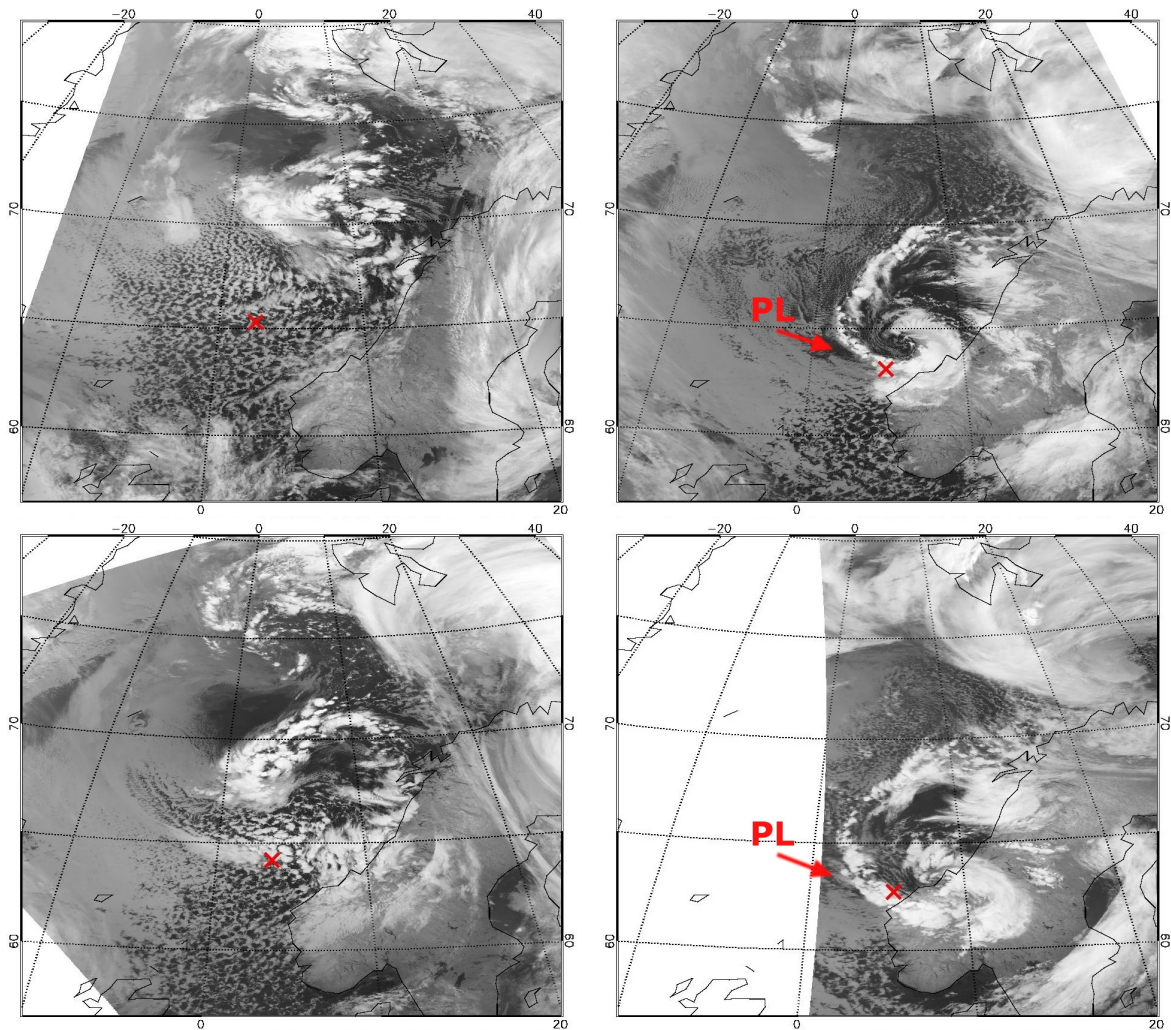


Figure 4.8: MODIS thermal infrared satellite images showing the lifecycle of the polar low as well as the conditions prior to its development on (top left: 1:55 UTC 29 November 2005; bottom left: 11:35 UTC 29 November 2005; top right: 21:05 UTC 29 November 2005; bottom right: 1:00 UTC 30 November 2005). The red crosses mark the location of weather ship M at the time closest to the MODIS observations. PL stands for “polar low”.

4 Multi-sensor view of subsynoptic storm systems

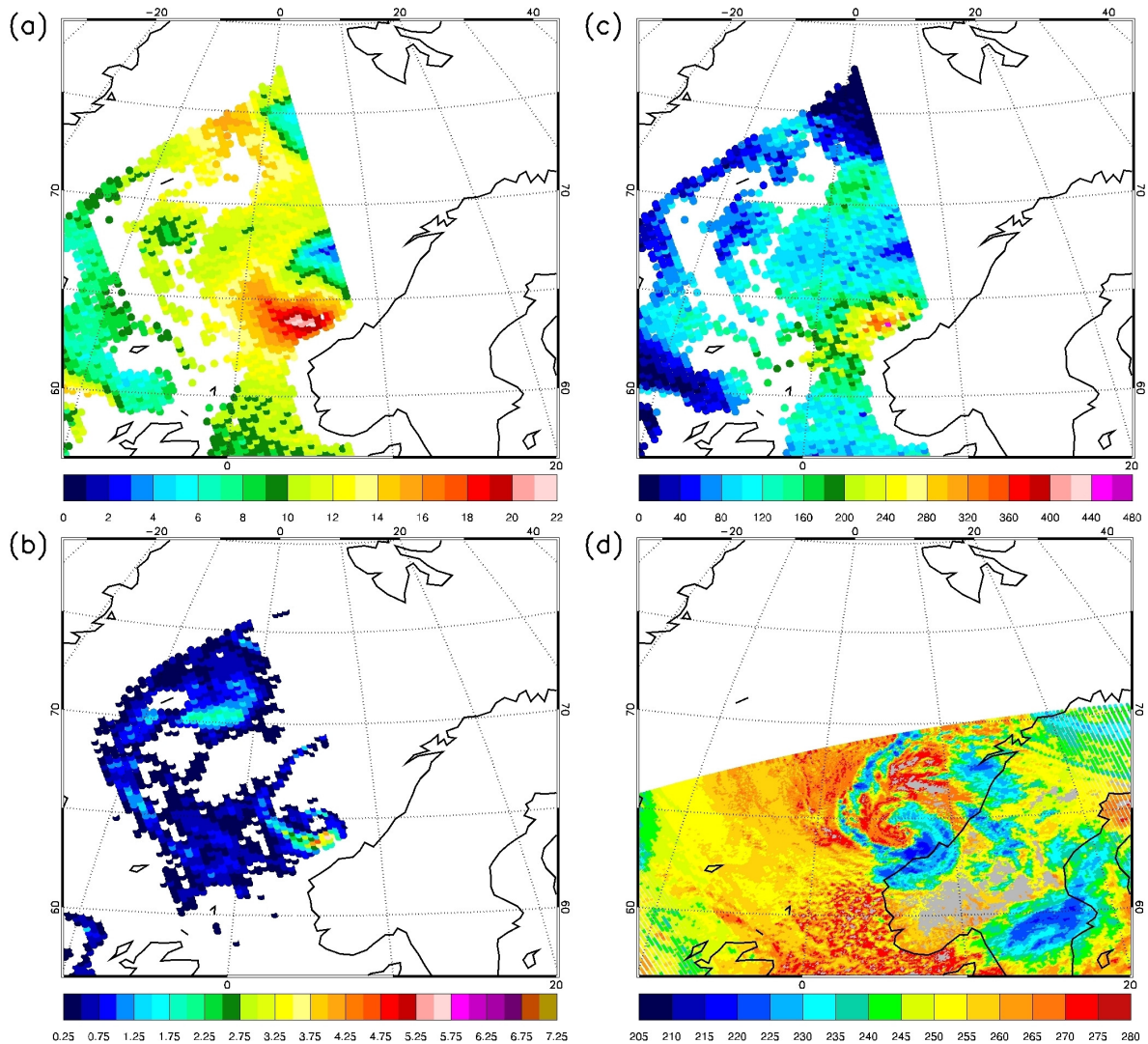


Figure 4.9: Satellite derived atmospheric parameters on 29 November 2005 for the time closest to the mature stage of the polar low showing (a) wind speed [m/s], (b) precipitation rate [mm/hr], (c) latent heat flux [W/m^2] from HOAPS (DMSP F15) at 19:55 UTC and (d) cloud top temperature [K] from MODIS at 21:00 UTC.

the outbreak of cold air over relatively warm water. At 11:35 UTC on 29 November 2005 the cloud cluster had grown to the vortex shown in the bottom left panel of Figure 4.8. Towards the evening, the head of this vortex reached its tail. This merging resulted in the rapid development of the comma shaped polar low shown in the top right panel of Figure 4.8 in its mature stage at 21:05 UTC on 29 November 2005. During the next hours, the polar low decayed as it propagated eastwards over land (see bottom right panel of Figure 4.8).

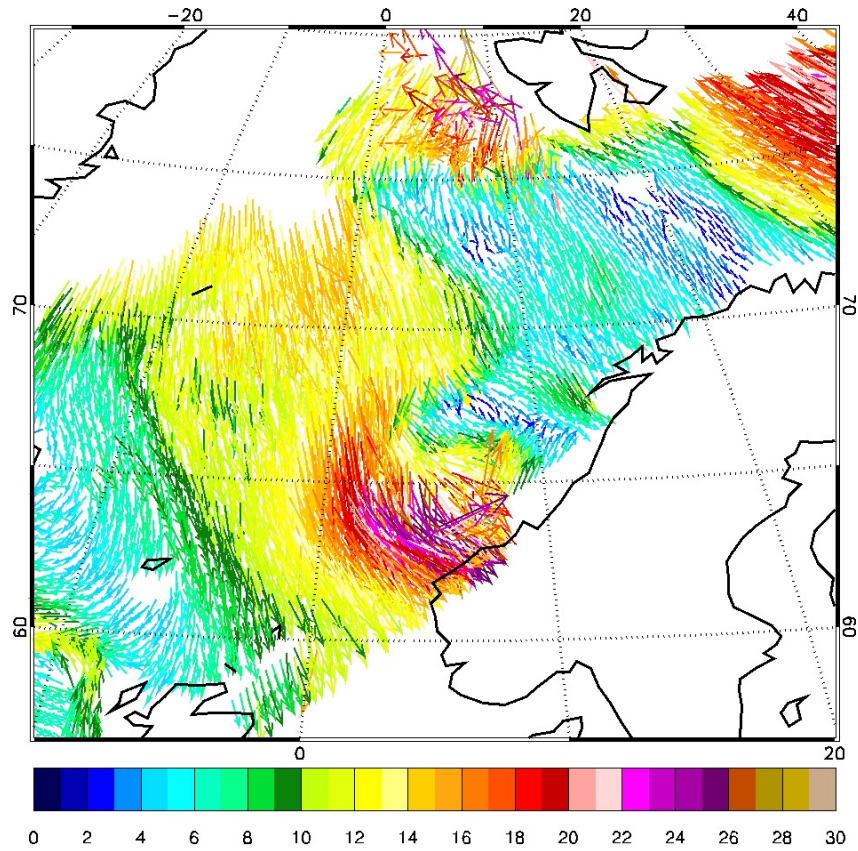


Figure 4.10: Wind speed [m/s] and wind direction from QuikSCAT at 20:11 UTC 29 November 2005.

4.3.2 Mature stage

Figure 4.9 shows fields of several atmospheric parameters closest to the mature stage of the polar low derived from HOAPS and MODIS data. The polar low reached wind speeds up to 22 m/s, precipitation rates up to 5.75 mm/hr, latent heat fluxes up to 445 W/m^2 and cloud top temperatures down to 215 K. The latter corresponds to a MODIS cloud top pressure (not shown) of 330 hPa. Regarding the frequency distributions of all these atmospheric parameters for polar lows detected in 2004 and 2005 shown in Figure 4 of chapter 2, the polar low discussed in the present chapter is one of the stronger cases included in the 2-year data set.

In addition to the HOAPS wind speeds shown in Figure 4.9 (a), wind speed and wind direction from QuikSCAT derived closest to the mature stage of the polar low are shown in Figure 4.10. The polar low reached QuikSCAT wind speeds up to 27 m/s. Although the time difference between the HOAPS and the QuikSCAT observation is only 16 minutes,

4 Multi-sensor view of subsynoptic storm systems

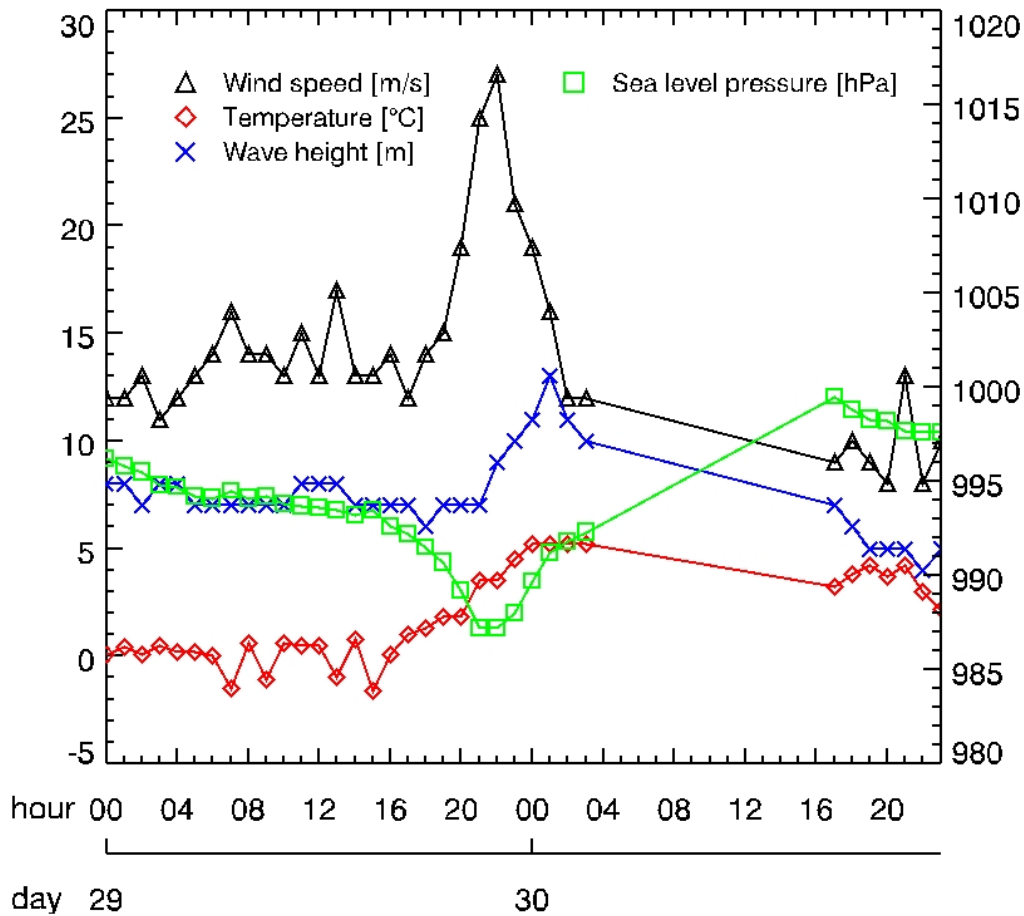


Figure 4.11: Observations from weathership M for 0:00 UTC 29 November 2005 to 23:00 UTC 30 November 2005 derived from VOS data.

the QuikSCAT wind speed maximum is 5 m/s larger than the HOAPS wind speed maximum. However, the QuikSCAT value agrees well with a wind speed maximum reported by a VOS ship which will be described below. The deviations between HOAPS and QuikSCAT wind speeds may result from different satellite observation times, resolutions and frequencies of the remote sensors. In Figure 4.10 the sea ice is indicated by missing QuikSCAT data to the east of Greenland. The QuikSCAT wind directions show that the polar low is located in an outbreak of cold air directed from the ice towards the southern part of Norway. The outbreak of cold air above the relatively warm ocean close to the Norwegian coast is a favourable condition for intense air-sea interaction. This agrees well with the large latent heat fluxes derived from HOAPS which were described above.

Weathership M was hit by the polar low in the evening of 29 November 2005. The

location of the ship is marked by a red cross in the MODIS thermal infrared satellite images shown in Figure 4.8. The ship observations are shown in Figure 4.11. Between 16:00 UTC and 22:00 UTC on 29 November 2005, the wind speed increased from 14 m/s to 27 m/s and the sea level pressure decreased from 997 hPa to 992 hPa. This corresponds to a wind speed increase of 13 m/s and a pressure drop of 5 hPa in 6 hours. After 22:00 UTC, wind speed and sea level pressure changed to the incipient values in the same period of time. Temperature and wave height reached a maximum of 5°C and 13 m at 1:00 UTC on 30 November 2005, respectively. The pronounced temperature rise of about 5°C from 16:00 UTC on 29 November 2005 to 1:00 UTC on 30 November 2005 shows that the polar low possessed a warm core. The strong fluxes of latent heat revealed by the HOAPS data which were reached close to the mature stage of the polar low (see above) might have contributed to this rise in air temperature.

4.3.3 Large scale circulation

The large scale circulation during the mature stage of the polar low is represented by the NCEP R-2 fields at 18:00 UTC 29 November 2005 shown in Figure 4.12. A synoptic scale low is situated over Scandinavia. There is higher pressure over Greenland. The resulting northerly flow over the Norwegian Sea agrees well with the QuikSCAT wind directions described above. An upper level cold low which reaches minimum GPH_{500} values of 5000 gpm and T_{500} values down to 227 K is located over Scandinavia. It follows from the inspection of NCEP fields prior to 18:00 UTC 29 November 2005 (not shown) that this cold upper level disturbance originated from Spitsbergen and moved towards the Norwegian Sea. This resulted in the development of a $SKT-T_{500}$ difference over the Norwegian Sea which reaches 52 K at 18:00 UTC 29 November 2005. The location of this maximum $SKT-T_{500}$ difference is coincident with the location of the polar low shown by the MODIS satellite image in the top right panel of Figure 4.8. The location of the polar low is also well represented by an IPV_{315} maximum of 9 PVU in NCEP R-1 (not shown). The maxima and minima described above are more pronounced than the values that are most often reached during polar low events (see Figure 5 of chapter 3). The minimum in GPH_{500} is 30 gpm lower, the minimum in T_{500} is 6 K lower, the maximum in $SKT-T_{500}$ is 4 K higher and the IPV_{315} maximum is 2 PVU higher than the typical value.

Overall, the NCEP fields agree well with the typical large scale circulation associated with western polar lows shown in the top left panel of Figure 6 in chapter 3. However, the direction of the surface flow over the Norwegian Sea which is directed from the ice towards the sea, disagrees with the direction of the mean surface flow which was found to be directed parallel to the ice edge (see Table 1 of chapter 3). The direction of the

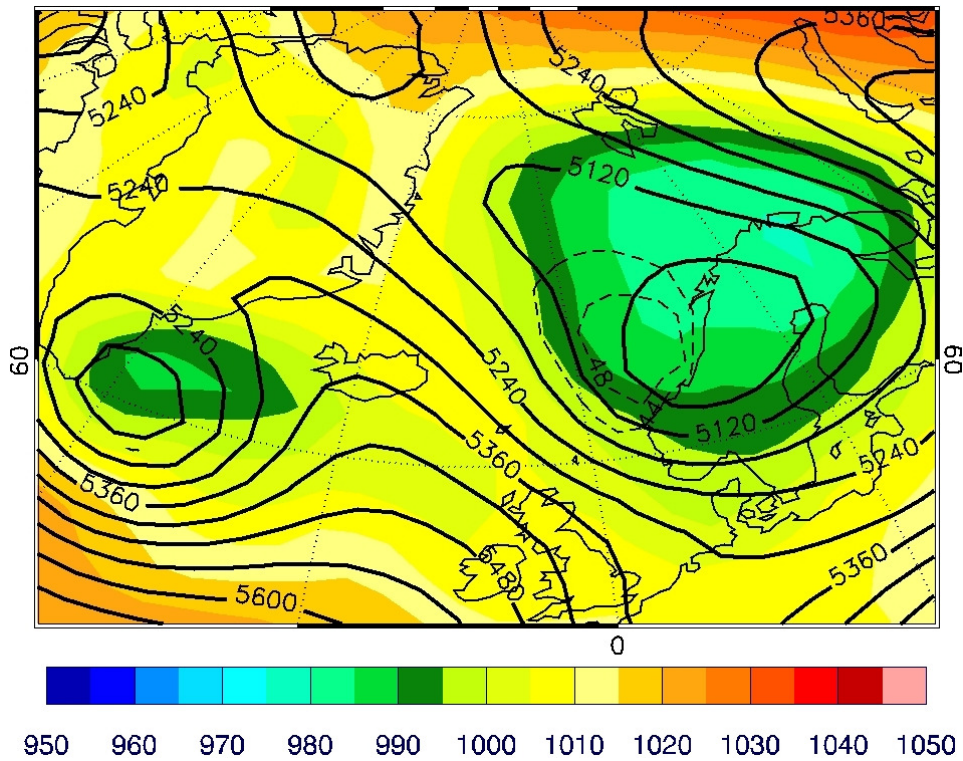


Figure 4.12: NCEP R-2 fields showing the large scale conditions during the polar low event at 18:00 UTC 29 November 2005. The coloured contours show sea level pressure [hPa], the black contours show GPH₅₀₀ [gpm] and the black dashed contours show SKT-T₅₀₀ ≥ 44K.

large scale flow associated with an individual polar low event can deviate to some extent from the direction of the mean flow.

4.4 Case 3: 6 February 2006

A polar mesocyclone developed over the Norwegian Sea on 6 February 2006. In the following the initial development, mature stage, large scale circulation and reverse shear conditions are described.

4.4.1 Initial development

On 6 February 2006 a polar mesocyclone developed from an old synoptic scale cyclone that moved northeastwards from the region between Iceland and the northernmost part of Great Britain towards the Norwegian Sea. This is illustrated by the sequence of thermal infrared AVHRR images in Figure 4.13.

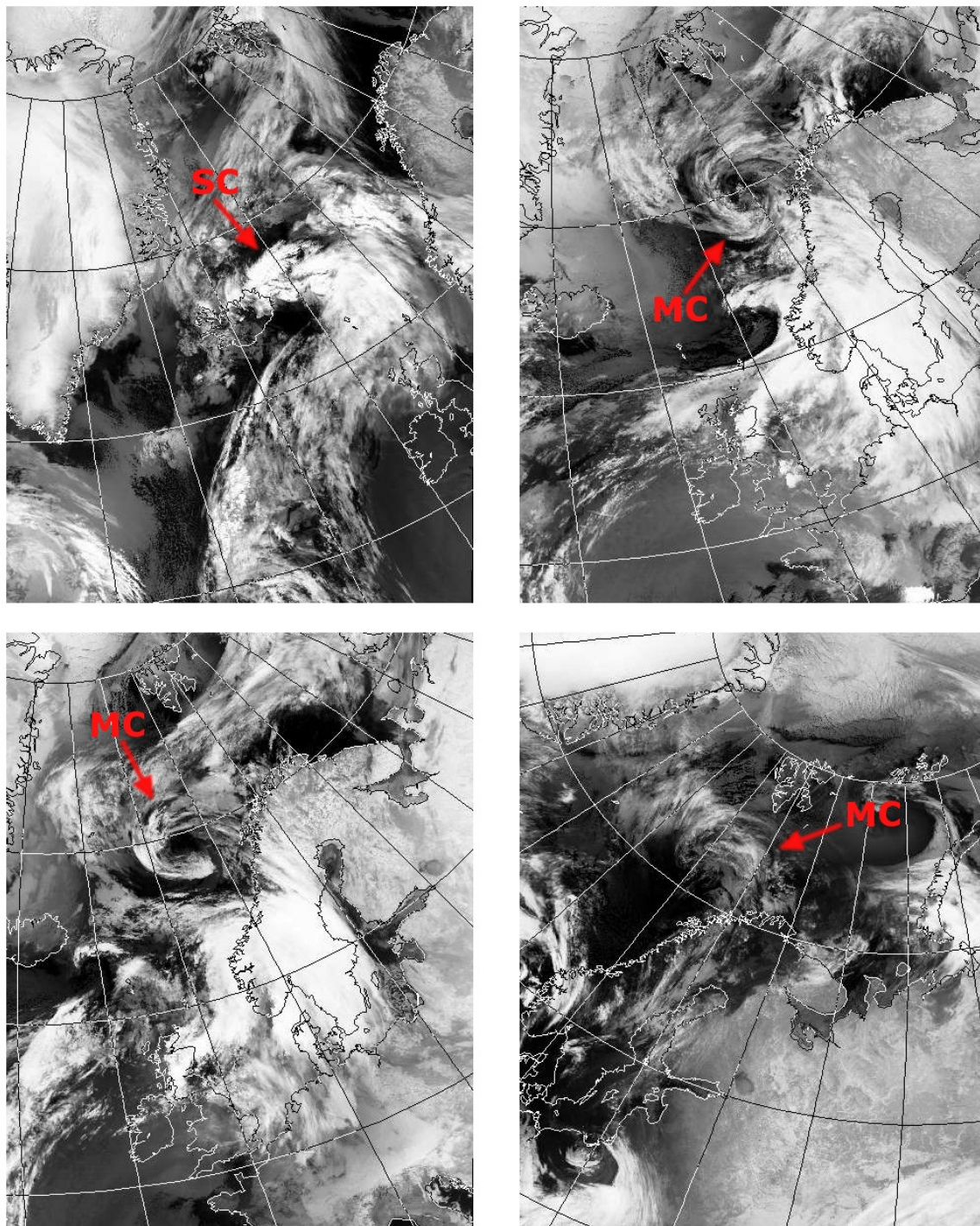


Figure 4.13: Thermal infrared AVHRR images showing the development of the polar mesocyclone (top left: 4:31 UTC 5 February 2006; bottom left: 2:40 UTC 6 February 2006; top right: 11:33 UTC 6 February 2006 (mature stage); bottom right: 10:45 UTC 7 February 2006). SC stands for “synoptic scale cyclone” and MC for “mesocyclone”. (Image courtesy of the NERC Satellite Receiving Station, University of Dundee, Scotland.)

4 Multi-sensor view of subsynoptic storm systems

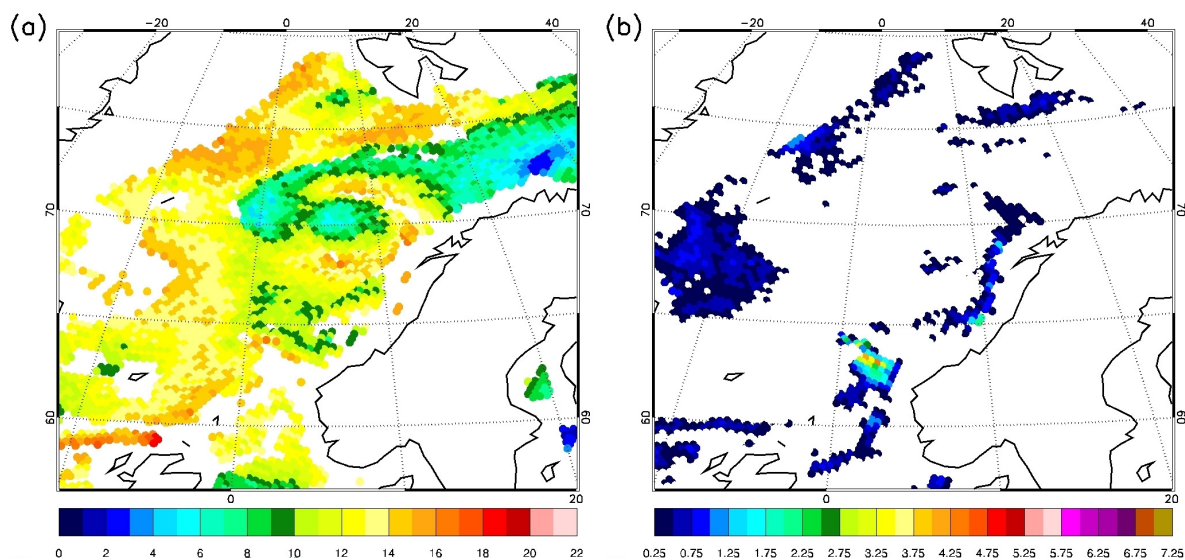


Figure 4.14: Wind speed [m/s] (a) and precipitation [mm/hr] (b) from HOAPS (DMSF F15) on 6 February 2006 from 8:54 UTC to 10:42 UTC.

The top left panel shows the synoptic scale cyclone with a center to the east of Iceland in the early morning of 5 February 2006. During this day, the decaying synoptic scale cyclone moved further northeastwards over the Norwegian Sea and the polar mesocyclone shown in the bottom left panel of Figure 4.13 at 2:40 UTC on 6 February 2006 developed. The mesocyclone further intensified and reached its mature stage at 11:33 UTC (top right panel). The center of the spiral shaped polar mesocyclone is located near 8° East and 70° North. This polar mesocyclone is too large to be regarded as a polar low, since the diameter is about 1400 km. The polar mesocyclone remained nearly stationary during the next hours and completely lost its spiral structure by 10:45 UTC on 7 February 2006 (see bottom right panel of Figure 4.13).

4.4.2 Mature stage

Close to its mature stage the polar mesocyclone reached HOAPS wind speeds of 17 m/s and HOAPS precipitation rates of 1.75 mm/hr (see Figure 4.14). It should be noted that the latent heat flux from HOAPS is not available for 2006 and therefore can not be shown. The AATSR and the Envisat altimeter also spotted the polar mesocyclone close to its mature stage. Figure 4.15 shows cloud top temperature from AATSR and the track of the Envisat altimeter at 10:45 UTC on 6 February 2006. The mesocyclone reached minimum cloud top temperatures of about 230 K. The altimeter track crossed the mesocyclone to the east of its center. The corresponding profiles are given in Figure 4.16. A maximum

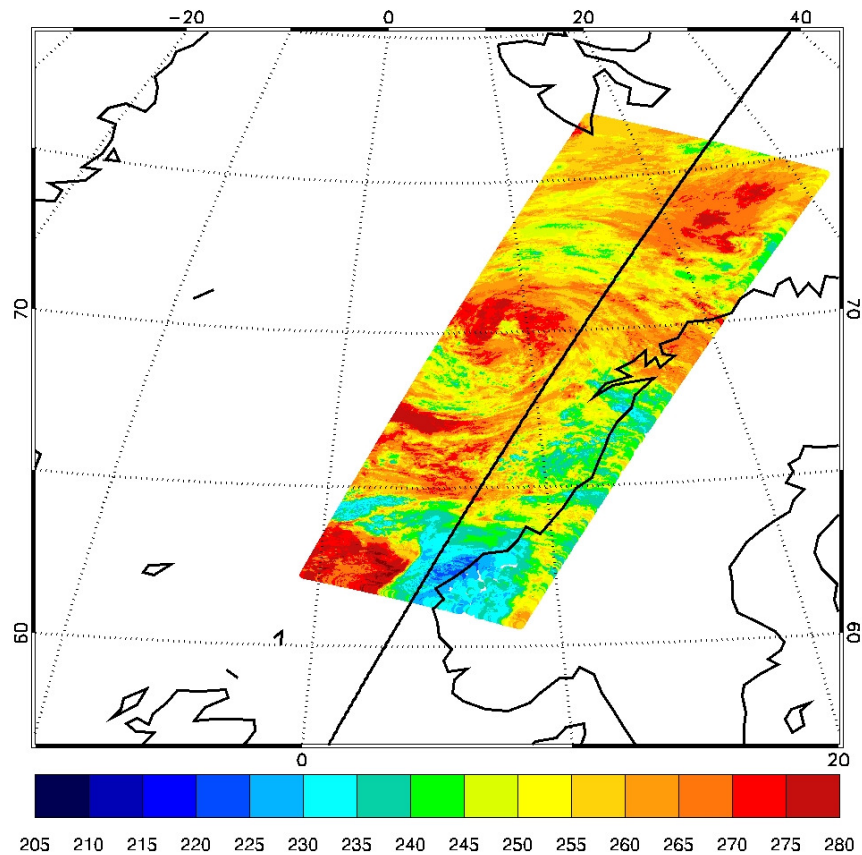


Figure 4.15: Cloud top temperature [K] from AATSR and the track of the Envisat altimeter (black line) at 10:45 UTC 6 February 2006.

in wind speed of 16 m/s and a maximum in significant wave height of 5 m is reached near 12° East.

4.4.3 Large scale circulation

Figure 4.17 shows NCEP data at 12:00 UTC 6 February 2006 which corresponds to the mature stage of the polar mesocyclone. The mesocyclone is associated with the sea level low over the Norwegian Sea. In contrast to the polar low events described above, this rather large mesocyclone is directly resolved by the Reanalysis data due to its comparatively large size. The SKT- T_{500} difference only reaches maxima of 40 K. This maximum is located near an upper level trough which is situated to the west and southwest of the cyclone center. A trailing trough at the sea level is indicated to the southwest of the cyclone center, due to the movement of the decaying synoptic scale cyclone from which the polar mesocyclone developed.

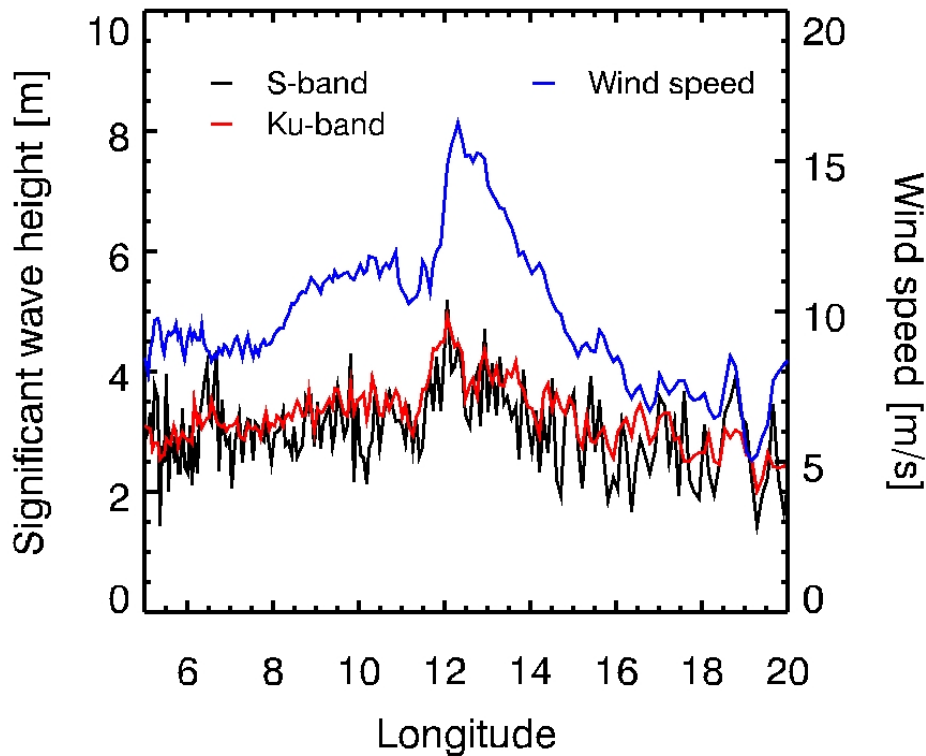


Figure 4.16: Envisat altimeter profiles at 10:45 UTC 6 February 2006 corresponding to the track shown in Figure 4.15.

4.4.4 Reverse shear baroclinicity

There is strong evidence that reverse shear baroclinicity played a major role for the genesis of the polar mesocyclone. As described in chapter 2 and 3, the term reverse shear refers to a situation where the direction of the thermal wind is opposite to the wind direction at the steering level and the magnitude of the horizontal wind decreases with height. *Duncan* (1978) was the first one who identified reverse shear baroclinicity as an important instability mechanism that contributes to many polar low developments. The concept of reverse shear development is illustrated in Figure 4.18. In contrast to classical baroclinic cyclones, the warm air lies to the left of the background flow and the cold air lies to the right. The effect of horizontal advection is such that warm air rises behind the disturbance, while cold air subsides in front of it. This builds a thermally direct circulation that gains kinetic energy at the expense of available potential energy (*Rasmussen and Turner, 2003*). *Kolstad* (2006) noted that when storms propagate from

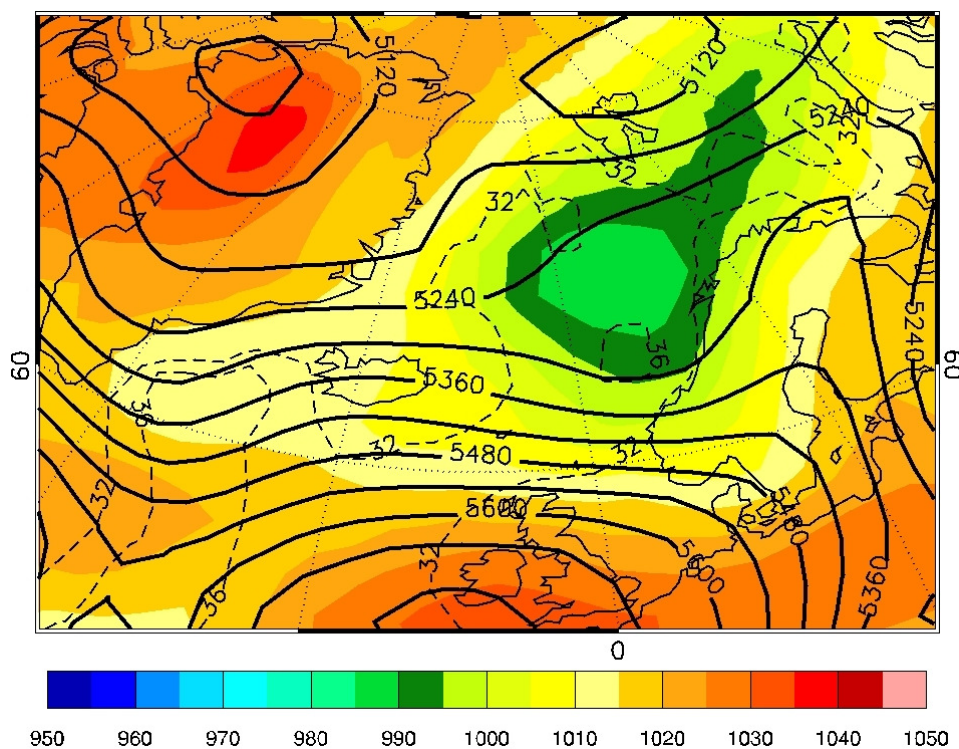


Figure 4.17: NCEP R-2 fields for 6 February 2006 12:00 UTC. The coloured contours show sea level pressure [hPa], the black contours show GPH_{500} [gpm] and the black dashed contours show $SKT-T_{500} \geq 32K$.

the southwest into the Norwegian and Barents Seas, the proximity of the Arctic ice to their north frequently leads to low static stability and reverse shear in the northerly flow following such lows.

To identify reverse shear conditions for the polar mesocyclone discussed in this chapter, the wind direction at 850 hPa, which is assumed to be the steering level of the cyclone, is compared to the direction of the thermal wind in the 700-925 hPa layer using NCEP R-2 data. A similar method was applied to ERA-40 data by *Kolstad* (2006). In the present thesis, the thermal wind was derived from the actual wind field rather than from the geostrophic wind. It is assumed that the effect of friction over open water and sea ice is negligible in the 700-925 hPa layer so that the actual wind is close to the geostrophic one.

Figure 4.19 shows the direction of the thermal wind and the direction of the wind at the steering level on 6 February 2006 at 12:00 UTC. To the north and to the northwest of the cyclone center, the thermal wind is in the opposite direction as the wind at the steering level. It follows from Figure 4.20, which shows the difference between wind

4 Multi-sensor view of subsynoptic storm systems

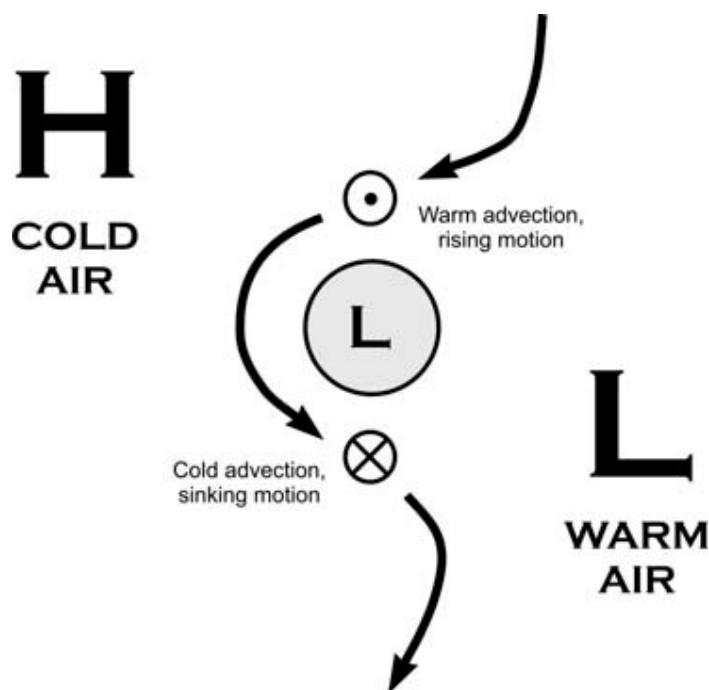


Figure 4.18: Schematic illustration of a reverse shear cyclone development from *Kolstad* (2006). The steering level is seen from above and the pressure decreases to the right of the picture. The cyclone under development is shown in the center of the image. The background geostrophic flow has a downward direction. The warm air lies to the left of this flow so that the thermal shear is reversed. A direct thermal circulation is ensured by warm advection and rising motion upstream of the low combined with cold advection and sinking motion downstream of the low.

speed at 700 hPa and 925 hPa, that the wind at these locations is decreasing with height. Therefore, reverse shear baroclinicity is present in these regions. Furthermore, Figure 4.19 reveals that there is wind veering and therefore warm advection to the east and the south of the cyclone center, while there is wind backing and therefore cold advection to the northeast, north and west of it. A QuikSCAT image at 5:00 UTC on 6 February 2006 (see Figure 4.21), which is the QuikSCAT image closest to the mature stage of the polar mesocyclone, shows that there is convergence of low level winds to the north of the cyclone center. The strongest convergence occurs near 10° East and 74° North. It is most likely that rising motion occurs at this location. The strongest wind speeds of 19 m/s are reached to the east of the cyclone center. The presence of sea ice is indicated by the missing QuikSCAT data over the Fram Strait. This suggests that cold air over sea ice is located to the right of the northerly flow over the Fram Strait and the Norwegian Sea. Moreover, there is divergence of low level winds near -4° East and 66° North indicating sinking motion. The view of the polar mesocyclone gained through

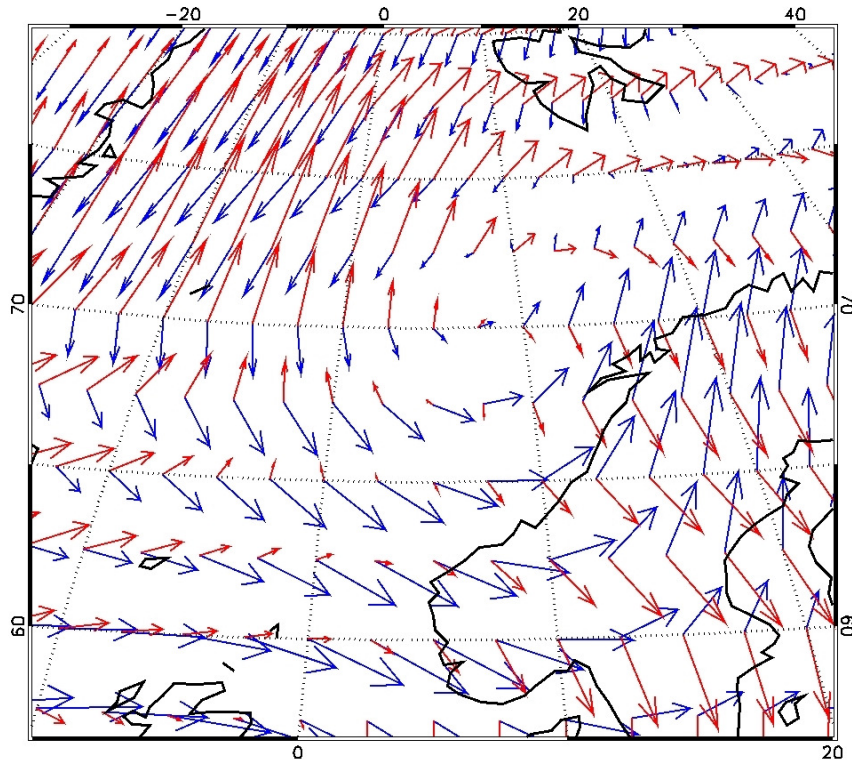


Figure 4.19: Wind direction at the 850 hPa level (blue arrows) and direction of the thermal wind in the 700-925 hPa layer (red arrows) at 12:00 UTC 6 February 2006 derived from NCEP R-2.

the NCEP and QuikSCAT data agrees well with the schematic illustration of a reverse shear cyclone given in Figure 4.18.

The strong convergence line to the north of the cyclone center present in the QuikSCAT wind field coincides with the region of strong SST gradients between the East Greenland current and the Norwegian Atlantic current. This follows from the comparison of the QuikSCAT wind field (Figure 4.21) with the AMSR-E SST derived from ascending passes on 6 February 2006 shown in Figure 4.22. Since the temperature of the air at the sea level is influenced by SST, this might enhance the temperature contrast between cold air to the right and warm air to the left of the northerly flow over the Fram Strait and the Norwegian Sea.

4.5 Summary and concluding remarks

The development and lifecycle of three subsynoptic storm systems over the Norwegian Sea has been studied by combined use of active and passive satellite remote sensing data,

4 Multi-sensor view of subsynoptic storm systems

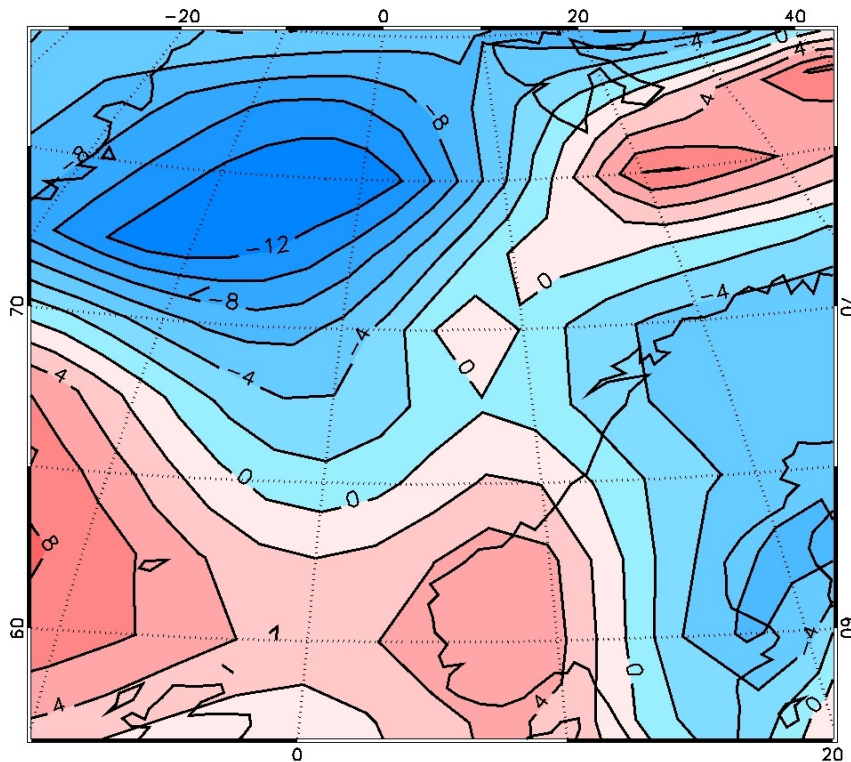


Figure 4.20: Difference between wind speed at 700 hPa and wind speed at 925 hPa at 12:00 UTC 6 February 2006 derived from NCEP R-2. Blue colour marks negative values, red colour marks positive values.

ship observations and Reanalysis data.

Firstly, a dual polar low event was investigated which was triggered by the arrival of an upper level cold low. The polar lows were part of one merry-go-round system and propagated in a cyclonic sense around its center. HOAPS data indicates that air-sea interaction contributed to the intensification of SPL, probably due to an increase of SST as it propagated eastwards towards the Norwegian coast. Secondly, one of the most intense polar low events from the 2-year data set has been studied. Ship observations of this polar low show a pronounced increase in wind speed and temperature as well as a pronounced pressure drop. Large HOAPS latent heat fluxes suggest that air-sea interaction might have contributed to the formation of a warm core. The typical large scale circulation during western polar low events (Figure 6 and Table 1 of chapter 3) agrees well with the NCEP fields for both polar low events studied in the present chapter. Both of the polar low events developed in a northerly surface flow caused by a large scale low over the Norwegian Sea and a high over Greenland. Both polar low developments are associated with the arrival of a cold upper level disturbance as well as the development of a large SKT- T_{500} difference over the Norwegian Sea. Finally, a polar mesocyclone

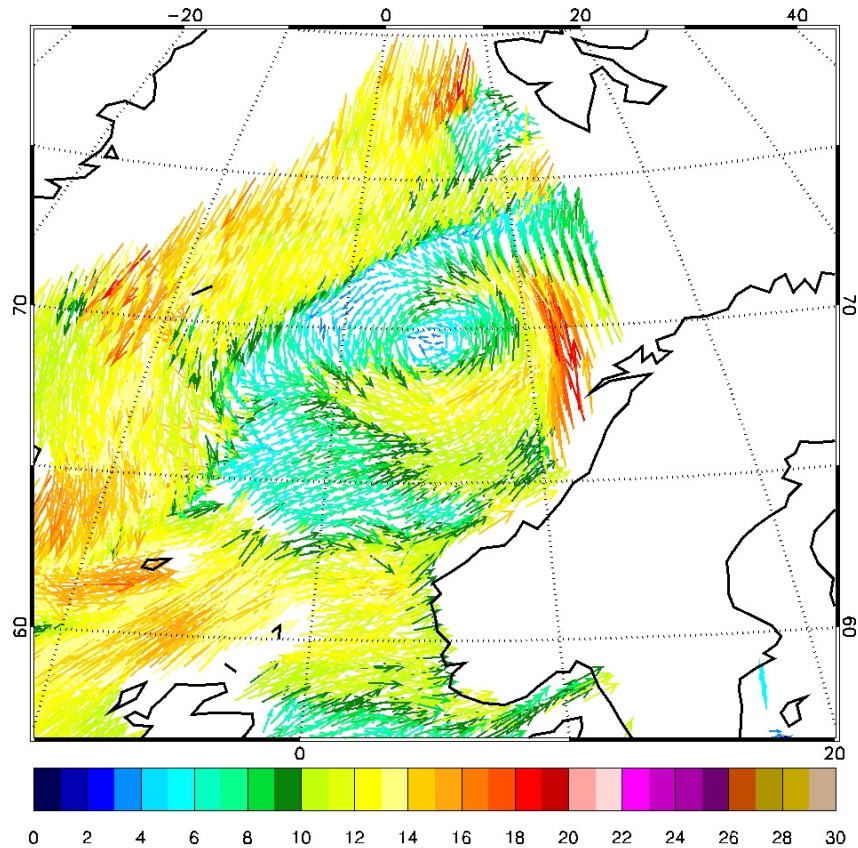


Figure 4.21: Wind speed [m/s] and wind direction from QuikSCAT at 5:00 UTC 6 February 2006.

has been investigated. NCEP and QuikSCAT data strongly suggest that reverse shear baroclinicity contributed to the genesis of the mesocyclone.

The case studies presented above have shown that the lifecycle of subsynoptic storm systems is well represented by using several sources of satellite data. A more detailed view of the structure of three subsynoptic cyclones has been achieved based on passes of different satellites that overlap not only for the location of the cyclones but also in observation time. Especially the combined use of active and passive remote sensing data provides information about many parameters e.g., wave height, surface wind speed with high resolution, latent heat flux and cloud top temperature. However, the availability of coinciding satellite observations for polar low related studies is limited. This is due to the small scale and short lifetimes of polar lows and the comparatively low spatial coverage of active remote sensors like altimeters or synthetic aperture radars. Moreover, it is hard to draw exact conclusions about the dynamical processes that underlie the development of the cyclones from satellite data alone. Regarding the subsynoptic cyclone cases studied in this chapter, further conclusions about dynamical forcing mechanisms may follow from

4 Multi-sensor view of subsynoptic storm systems

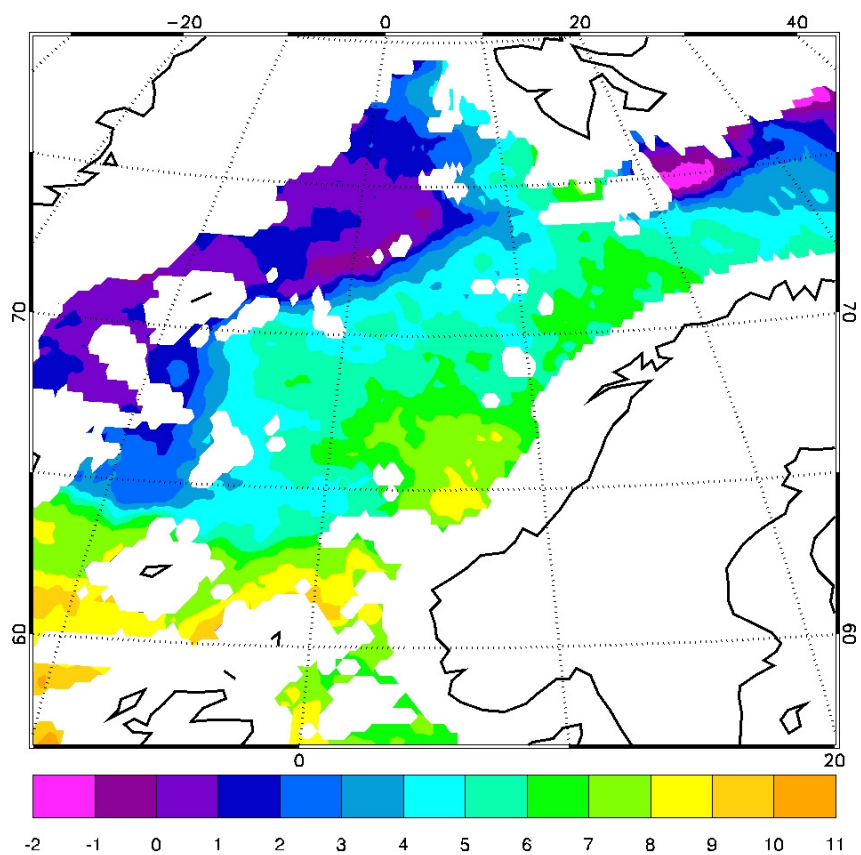


Figure 4.22: SST [K] from AMSR-E ascending passes for 6 February 2006.

simulating these cases with a high resolution model. The various satellite observations could aid in testing the quality of the model results.

5 Comparison of satellite wind speeds and their error due to precipitation

The weather and climate of the extratropical latitudes are dominated by synoptic scale cyclones. But also mesoscale cyclonic systems of various dimensions and intensity are observed over the extratropical oceans, some of which are of large impact on the weather and climate of the European coastal regions and even continental Europe. Especially polar lows are often associated with strong winds and heavy precipitation. In the preceding chapter, a more detailed view of individual subsynoptic storm systems has been achieved by combined use of several active and passive satellite remote sensors. This combined use should also give insight into the accuracy of satellite derived atmospheric parameters in extreme weather situations. The focus of this chapter is on co-located wind speeds (u_{10}) in severe storm systems including polar lows, atmospheric fronts and comma-clouds over the eastern North Atlantic Ocean. E.g., the dual polar low event on 15 March 2005 (see chapter 4) is part of the wind speed comparisons which will be presented below. Passive microwave wind speeds from HOAPS are compared to wind speeds from the QuikSCAT scatterometer, the Jason-1 altimeter and the Envisat altimeter. The retrieval of satellite wind speeds in the presence of precipitation is crucial and will be evaluated through this combination technique. The influence of precipitation on satellite wind speeds in principle and co-location methods are described in section 5.1, followed by the results in section 5.2.

5.1 Influence of rain and co-location methods

5.1.1 HOAPS-3

The HOAPS-S data set is used here, which contains wind speeds in the original SSM/I scan resolution (that is 50 km) for every individual satellite. Horizontally polarized channels are more sensitive to the wind speed signal than vertically polarized channels, particularly at the SSM/I incidence angle (*Raytheon Systems Company*, 2000). Since surface roughness increases brightness temperatures, any phenomenon that roughens the

5 Comparison of satellite wind speeds and their error due to precipitation

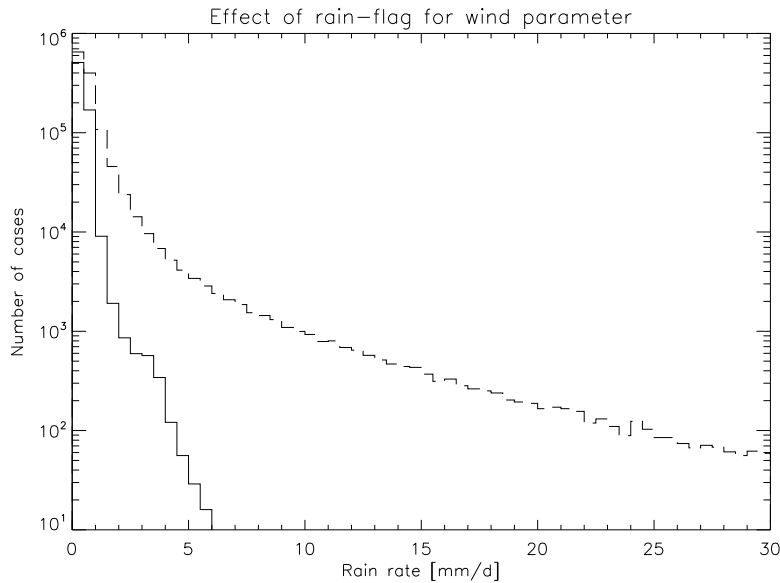


Figure 5.1: Number of pixels in bins of 0.5 mm/d width against rain rate resulting from 15 randomly selected days of scan data of all different SSM/I radiometers. The dashed line shows the number of all pixels containing rain rates > 0 . The solid line shows the number of pixels for which no atmospheric contamination was detected. (The image was kindly provided by Axel Andersson from the University of Hamburg.)

ocean surface can result in erroneous wind speeds. Therefore wind speed is not accurate in heavy rain, and even light rain can degrade the signal. Additionally, virga and cloud water affect the SSM/I signal. Pixels containing substantial atmospheric contamination (rain) are filtered in HOAPS-3 to avoid misdetection of wind speeds. The detection is done by brightness temperature thresholds for 19 and 37 GHz channels. If one of these thresholds is exceeded, the corresponding pixel is flagged and wind values are not calculated. Figure 5.1 shows the efficiency of this procedure. The number of pixels for which no atmospheric contamination is detected and which are therefore not flagged is decreasing very fast by several orders of magnitude with increasing rain rates, indicating the performance of the filter. For rain rates above 6 mm/h all pixels are flagged.

5.1.2 Dual frequency altimeters

The main effect of rain on altimeter data is the attenuation of the pulse through absorbing rain drops which increases with frequency (*Goldhirsh and Rowland, 1982*). Additionally, rain roughens the sea surface and changes its radar cross section. The Envisat

5.2 Comparison of satellite derived wind speeds

and Jason-1 satellites carry microwave radiometers to correct the atmospheric path delay due to water vapor. To identify pixels contaminated by rain, rain flags are assessed from a combination of microwave radiometer liquid water and the difference between the backscatter derived from the altimeter frequencies. Altimeters provide high-resolution information since their footprint size is several kilometers. Regarding the co-location of altimeter and HOAPS wind speeds every HOAPS pixel that lies within a circle of 22.5 km radius from the center of the altimeter footprint is compared to the altimeter pixel. As for all other comparisons of satellite wind speeds presented below, the maximum time difference between co-located values is not larger than two hours.

5.1.3 QuikSCAT

The influence of rain on QuikSCAT wind speeds is comparable to that on altimeter data. However, the integration path through the atmosphere is longer since QuikSCAT incidence angles are greater than 45° . This implies that atmospheric effects to the Ku backscatter due to rain are more significant (*Chan et al.*, 2004). For co-location with HOAPS wind speeds every HOAPS pixel that lies within a circle of 22.5 km radius from the center of the QuikSCAT footprint is compared to the QuikSCAT pixel.

5.2 Comparison of satellite derived wind speeds

Scatterplots of satellite derived ocean surface winds for a region over the North Atlantic (40°W to 20°E longitude and 20°N to 80°N latitude) are produced based on several cases of comma clouds, atmospheric fronts and polar lows. A two-dimensional linear regression is applied to quantify the coherence between the different data sets. The correlation coefficient is calculated and a t-test is applied based on a level of significance of $\alpha=0.05$. The t-test shows that the results are significant in all cases presented.

Figure 5.2 shows wind speed from the Envisat altimeter against that from HOAPS. There is a good agreement between both datasets resulting in a high correlation of 0.949 ± 0.005 . The root mean squared error (rms) is 1.63 m/s and the bias 0.804 m/s. Wind speeds reach values above 15 m/s in most of the raining cases. For those wind speeds the agreement between HOAPS and the Envisat altimeter is very good. The main result is that the rms and bias are smaller for the raining cases than for the non-raining cases. The data points vary strongly for lower wind speeds, especially between 7 m/s to 15 m/s. A closer look at the data indicates that these are cases where the altimeter crossed atmospheric fronts, passed an ice-edge or has been close to the coast. The time difference between the HOAPS and the altimeter satellite passes may lead to differences

5 Comparison of satellite wind speeds and their error due to precipitation

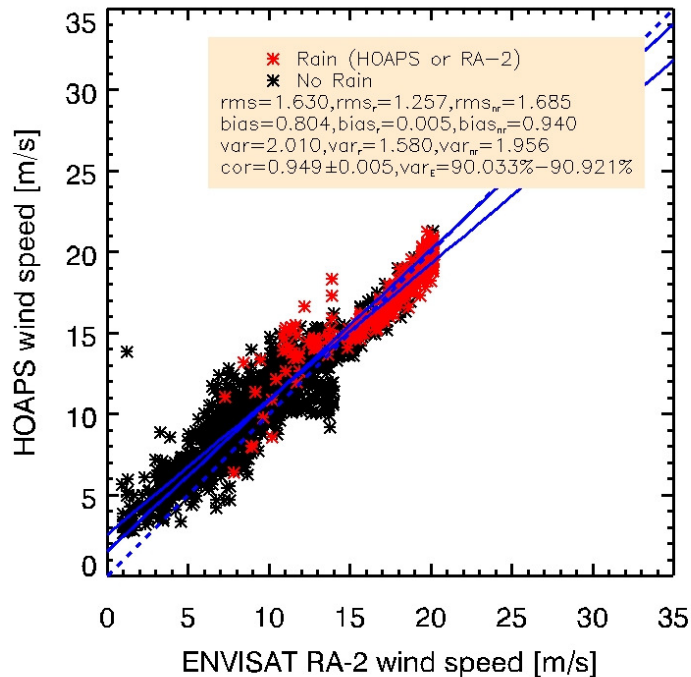


Figure 5.2: Envisat altimeter against HOAPS wind speed for 1752 co-located wind speeds over the eastern North Atlantic Ocean. Cases with HOAPS rain rates > 0 mm/hr or Envisat altimeter rain flag eq 1 are marked with red color. The dashed line is the reference line ($f(x)=x$). The other two black lines result from a two-dimensional linear regression. The root mean squared error (rms), the bias and variance of the error (var) are given for all data points, for the red data points (subscript r) and the black data points (subscript nr). The correlation coefficient (cor) and the variance explained by the two-dimensional linear regression (var_{ϵ}) are also given.

in wind speeds especially in those cases. Additionally, the different resolutions of the remote sensing systems lead to deviations in wind speeds. The sharp cut at 15 m/s may physically be related to the effect of sea foam which becomes dominant for values above 15 m/s. The two lines resulting from a two-dimensional linear regression show that HOAPS seems to overestimate low and underestimate high wind speeds compared to wind speeds from active remote sensors. This is also the case for the wind speed comparisons given below.

The Jason-1 altimeter against HOAPS wind speed is shown in Figure 5.3. The correlation between HOAPS and Jason-1 altimeter wind speeds is 0.912 ± 0.007 , which is

5.2 Comparison of satellite derived wind speeds

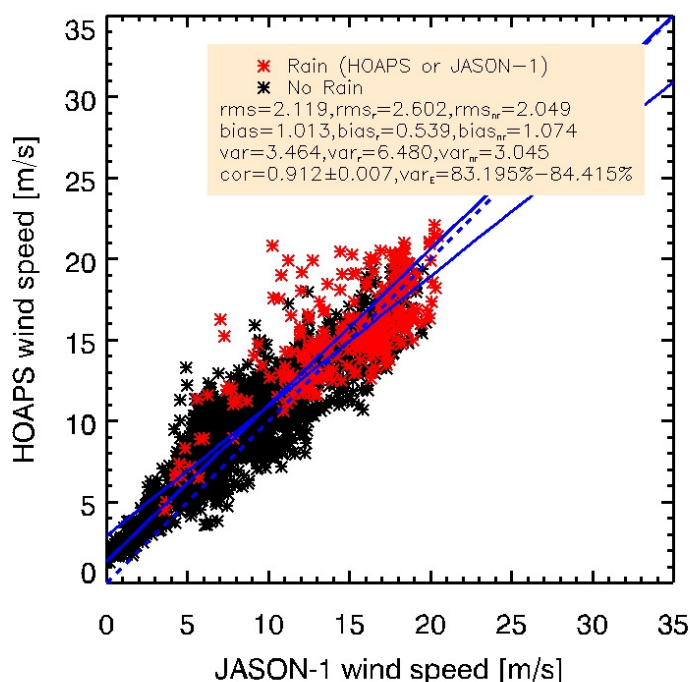


Figure 5.3: As in Figure 5.2, but for Jason-1 altimeter against HOAPS wind speed (2445 cases).

smaller than the correlation between HOAPS and the Envisat altimeter wind speeds. The rms is 2.119 m/s and the bias 1.013 m/s. The rms is larger for the raining than for the non-raining cases but the opposite is the case for the bias. The agreement between the different data sets is better for wind speeds below 5 m/s than for higher ones. In most of the raining cases the wind speed reaches values above 10 m/s. The largest deviations seem to be associated with rain. But since those are only very few cases, the error due to contamination of the signal by precipitation does not seem to be significant.

The QuikSCAT versus HOAPS wind speed is presented in Figure 5.4. The correlation between HOAPS and QuikSCAT wind speeds is 0.920 ± 0.008 . The wind speeds have a rms of 2.117 m/s and a bias of 0.133 m/s. The raining cases are spread almost equally over all wind speed values, although there is a tendency towards wind speeds above 10 m/s like in the comparison between HOAPS and the Jason-1 altimeter wind speeds. The rms and bias are higher in raining than in non-raining cases. Some of the largest deviations between HOAPS and QuikSCAT wind speed are again associated with rain but these are also few compared to the remaining cases.

5 Comparison of satellite wind speeds and their error due to precipitation

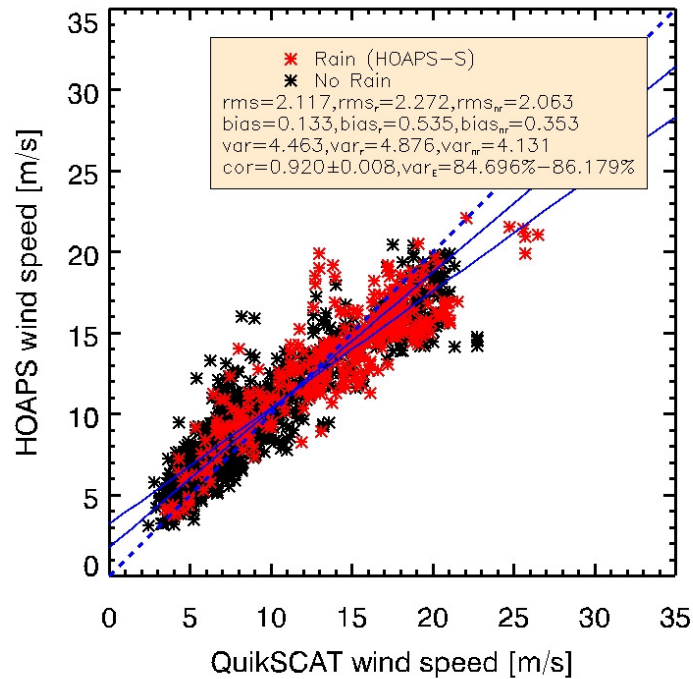


Figure 5.4: As in Figure 5.2, but for QuikSCAT against HOAPS wind speed (1399 cases).

5.3 Conclusions

Wind speeds from active remote sensing systems have been compared to passive microwave data from HOAPS for several comma cloud, atmospheric front and polar low cases over the eastern North Atlantic Ocean. The analysis has shown that HOAPS overestimates low and underestimates high wind speeds compared to the wind speeds derived from active remote sensors. A similar conclusion was drawn by *Winterfeldt et al.* (2008) who compared HOAPS wind speeds to buoy wind speeds in the eastern North Atlantic and the North Sea. They found that HOAPS shows an underestimation for higher wind speeds compared to the buoy data. In the present study, satellite derived wind speeds in high latitude severe storm systems over the eastern North Atlantic Ocean are associated with a rms of about 2 m/s. The best agreement was found between HOAPS and Envisat altimeter wind speeds with a correlation of 0.949 ± 0.005 and an rms of 1.630 m/s. Although undetected signal contamination by precipitation may result in large deviations between co-located wind speeds, the influence of precipitation on HOAPS wind speed does not seem to be significant since those cases are only few compared to the remaining cases. Therefore, regarding chapters 2 and 4, HOAPS is a convenient source to check

5.3 Conclusions

the wind speed criterion for polar lows as well as for case studies of high-latitude storm systems. Deviations in wind speeds basically result due to different satellite observation times and different resolutions of the remote sensors. The different frequencies and algorithms used for the derivation of wind speed and different viewing angles further contribute to the wind speed deviations.

5 Comparison of satellite wind speeds and their error due to precipitation

6 Summary and conclusions

The preceding chapters have shown that an improved understanding of polar lows can be gained from satellite remote sensing. In chapter 2, a 2-year data set of polar low events over the Nordic Seas resulting from a new satellite based detection scheme has been presented (*Blechschmidt, 2008*). Polar low detection is based on the combined use of thermal infrared AVHRR imagery and SSM/I derived wind speeds from the satellite climatology HOAPS. This is the first data set consistent with the widely used definition of polar lows by *Rasmussen and Turner [2003]* for the Nordic Seas. About 90 polar lows developed in the two years of the study with a maximum of polar low activity during the cold season. The main polar low genesis regions lie between Iceland and Finnmark in the Norwegian Sea, in the Barents Sea and in the lee region of Cape Farewell. Polar low activity was higher in the year 2004 than in 2005, mainly due to more frequent outbreaks of cold air into the study area in 2004. Statistics of polar low related atmospheric parameters show that these systems are short lived, small in size but very intense. The presented polar low data set builds a basis for studies about the dynamics leading to polar low formation and for the validation of mesoscale numerical models.

In chapter 3, the large scale atmospheric circulation during polar low events over the Nordic Seas has been investigated based on the 2-year data set (*Blechschmidt et al., 2009*). A classification system has been applied that divides the polar lows into four types (western polar lows, eastern polar lows, Greenland lee polar lows and storm track polar lows). Type specific large scale atmospheric circulation patterns were identified from NCEP Reanalysis data. At least to the author's knowledge, such an analysis has not been carried out for the whole Nordic Seas region in any previous study. The evaluated polar low types show distinct, characteristic large scale circulation patterns of sea level pressure, upper level geopotential height and of the difference between the skin temperature of the ocean and upper level temperature. This supports previous studies which used variables like GPH_{500} , T_{500} and $SKT-T_{500}$ to detect polar lows or favourable conditions for polar low development (e.g., *Noer and Ovsted, 2003*; *Claud et al., 2007*; *Zahn and von Storch, 2008*). Eastern polar lows are found to be associated with a strong blocking situation caused by anomalously high pressure over Iceland and a synoptic scale low-pressure anomaly over the Barents Sea. A weaker blocking situation with

6 Summary and conclusions

an anomalous ridge over Greenland reaching into the Irminger Sea and a low-pressure anomaly over the Norwegian Sea favors the development of western polar lows. The location of upper level low-pressure anomalies relative to the locations of the related anomalies at the sea level shows that western and eastern polar lows form, on average, in a much less baroclinic large scale environment than Greenland lee and storm track polar lows. Typical values for polar low genesis are a GPH_{500} disturbance of 5030 gpm and a $SKT-T_{500}$ difference of 48 K. The upper level disturbances most often occur in the form of cold troughs or lows of the circumpolar vortex.

The development and lifecycle of two polar low events and one polar mesocyclone was investigated in detail in chapter 4. The large scale circulation for the two individual polar low events agrees well with the results presented in chapter 3. It was concluded that an improved insight into the structure of subsynoptic storms can be gained if a reasonable number of observations from active and passive satellite remote sensors are available. The multi-sensor approach presented could aid in validating high resolution models.

In chapter 5 passive microwave HOAPS wind speeds have been compared to wind speeds from active sensors for several high latitude storms including polar lows, comma clouds and atmospheric fronts. The influence of precipitation on satellite wind speeds was investigated. Only a minor influence of precipitation on HOAPS wind speeds was found. This confirms that HOAPS is indeed a suitable source to check the wind speed criterion for polar lows as well as for case studies of high-latitude storm systems.

It is desirable to extend the polar low data set presented in this thesis to a longer time period. An extended time series would for example allow to study correlations between polar low activity and the NAO (North Atlantic Oscillation). Since the detection of polar lows from satellite data is quite time-consuming, only a 2-year data set was compiled by *Blechschmidt* (2008). Moreover, a possible influence of the subjective way of polar low detection by eye on the polar low statistics should be investigated. A further question is, if it is possible to derive a probability for polar low occurrence by searching for the type specific characteristic large scale patterns that were identified from NCEP Reanalysis data. A preliminary experiment on this topic was carried out by the author which showed very promising results. However, more research has to be done to find out if the characteristic patterns might help to improve the forecasting of polar lows.

Bibliography

- Blechschmidt, A.-M. (2008), A 2-year climatology of polar low events over the Nordic Seas from satellite remote sensing, *Geophys. Res. Lett.*, *35*, L09815, doi:10.1029/2008GL033706.
- Blechschmidt, A.-M., S. Bakan, and H. Graßl (2009), Large-scale atmospheric circulation patterns during polar low events over the Nordic seas, *J. Geophys. Res.*, doi:10.1029/2008JD010865, in press.
- Bracegirdle, T., and S. Gray (2008), An objective climatology of the dynamical forcing of polar lows in the Nordic Seas, *International Journal of Climatology*, published online, doi:10.1002/joc.1686.
- Businger, S., and R. J. Reed (1989), Polar lows, in *Polar and Arctic Lows*, edited by P. F. Twitchell, E. A. Rasmussen, and K. L. Davidson, pp. 3–45, A. Deepak, Hampton, Virginia.
- Chan, S. H., R. R. Halterman, and D. G. Long (2004), Cross validation of Jason-1 and QuikSCAT wind speeds, in *Proc. IGARSS '04' Geoscience and Remote Sensing Symposium*, IEEE International.
- Claud, C., G. Heinemann, E. Raustein, and L. McMurdie (2004), Polar low le Cygne: Satellite observations and numerical simulations, *Quart. J. Roy. Met. Soc.*, *130*, 1075–1102.
- Claud, C., B. Duchiron, and P. Terray (2007), Associations between large-scale atmospheric circulation and polar low developments over the north atlantic during winter, *J. Geophys. Res.*, *112*, D12101, doi:10.1029/2006JD008251.
- Condron, A., G. R. Bigg, and I. A. Renfrew (2008), Modelling the impact of polar mesocyclones on ocean circulation, *J. Geophys. Res.*, *113*.
- Dannevig, P. (1954), *Meteorologi for flygere*, Aschehoug, Oslo.
- Duncan, C. N. (1978), Baroclinic instability in a reversed shear flow, *Met. Mag.*, *107*, 17–23.

Bibliography

- Forbes, G. S., and W. D. Lottes (1985), Classification of mesoscale vortices in polar air streams and the influence of the large-scale environment on their evolution, *Tellus, Ser. A*, *37*, 132–155.
- Goldhirsh, and Rowland (1982), A tutorial assessment of atmospheric height uncertainties for high-precision satellite altimeter missions to monitor ocean currents, *IEEE Trans. Geosci. Remote Sensing*, pp. 418–434.
- Grønås, S., and N. G. Kvamstø (1995), Numerical simulations of the synoptic conditions and development of arctic outbreak polar lows, *Tellus, Ser. A*, *47*, 797–814.
- Harold, J. M., G. R. Bigg, and J. Turner (1999), Mesocyclone activity over the north-east Atlantic. part 1: Vortex distribution and variability, *International Journal of Climatology*, *19*, 1187–1204.
- Kolstad, E. W. (2006), A new climatology of favourable conditions for reverse-shear polar lows, *Tellus, Ser. A*, *58*, 344–354.
- Noer, G., and M. Ovhd (2003), Forecasting of polar lows in the Norwegian and the Barents Sea, in *9th meeting of the EGS Polar Lows Working Group*, Cambridge, U.K.
- Rasmussen, E. A. (1979), The polar low as an extratropical CISK disturbance, *Quart. J. Roy. Met. Soc.*, *105*, 531–549.
- Rasmussen, E. A. (1989), A comparative study of tropical cyclones and polar lows, in *Polar and Arctic Lows*, edited by P. F. Twitchell, E. A. Rasmussen, and K. L. Davidson, pp. 3–45, A. Deepak, Hampton, Virginia.
- Rasmussen, E. A., and J. Turner (2003), *Polar lows: Mesoscale weather systems in the polar regions*, Cambridge University Press, Cambridge, U.K.
- Raytheon Systems Company (2000), SSM/I User’s Interpretation Guide.
- Reed, R. J. (1979), Cyclogenesis in polar airstreams, *Monthly Weather Review*, *107*, 38–52.
- Renfrew, I. A. (2003), Polar lows, in *The Encyclopedia of the Atmospheric Sciences*, vol. 3, edited by J. R. Holton, J. Pyle, and J. A. Curry, pp. 1761–1768, Academic Press.
- Shapiro, M. A., and L. S. Fedor (1986), The Arctic Cyclone Expedition, 1984: Research and aircraft observations of fronts and polar lows over the Norwegian and Barents Sea, Part 1, *Tech. Rep. 20*, The Norwegian Meteorological Institute, Oslo, 56 pp.

Bibliography

Winterfeldt, J., A. Andersson, C. Klepp, S. Bakan, and R. Weisse (2008), Comparison of HOAPS, QuikSCAT and buoy wind speed in the eastern North Atlantic and the North Sea, manuscript in preparation.

Zahn, M., and H. von Storch (2008), A long-term climatology of North Atlantic polar lows, *Tellus, Ser. A*, *60*, 620–63.

Zahn, M., H. von Storch, and S. Bakan (2008), Climate mode simulation of North Atlantic polar lows in a limited area model, *Geophys. Res. Lett.*

Danksagung

Diese Doktorarbeit wurde durch das von der HGF (Helmholtz Gemeinschaft) geförderte virtuelle Institut Extrop finanziert. Für die sehr angenehme Betreuung möchte ich mich bei Hartmut Graßl und Stephan Bakan bedanken. Sie haben durch konstruktive Kritik und Verbesserungsvorschläge wesentlich zu der vorliegenden Arbeit beigetragen. Desweiteren bedanke ich mich bei der HOAPS Gruppe (insbesondere bei Axel Andersson und Christian Klepp), der Extrop Gruppe sowie bei Matthias Zahn für die sehr hilfreichen Diskussionen und wertvollen Tipps. Ein weiteres wesentliches Dankeschön an Jenny Glashoff und auch an Biljana Krul für ihre tatkräftige Unterstützung bei der Erstellung der Statistiken. Ich bedanke mich bei Hans von Storch für den Vorschlag das erste Paper bei GRL einzureichen, was sicherlich eine gute Entscheidung war. Ein Dankeschön an Jochen Horstmann für die Berechnung des ASAR Windfeldes.

Desweiteren bedanke ich mich bei all den Personen, welche die in der vorliegenden Doktorarbeit verwendeten Satellitendaten (Dundee satellite receiving station, NASA), Reanalyse Daten (NOAA/OAR/ESRL PSD, CISL) und Schiffsdaten (CISL) auf ihren Webseiten zur Verfügung stellen. Die in dieser Arbeit verwendeten Envisat Daten wurden von der ESA über ein Category-1 Projekt (ID: 3898) bezogen.

Ganz herzlich bedanke ich mich bei meiner Familie, meinem Freundeskreis und natürlich (was hätte ich in den drei Jahren ohne ihn gemacht) bei Mike Boysen. Sie haben mich während der gesamten Zeit bestärkt und unterstützt.

Die gesamten Veröffentlichungen in der Publikationsreihe des MPI-M
„Berichte zur Erdsystemforschung“,
„Reports on Earth System Science“,
ISSN 1614-1199

sind über die Internetseiten des Max-Planck-Instituts für Meteorologie erhältlich:

<http://www.mpimet.mpg.de/wissenschaft/publikationen.html>

